





Article

N-Symmetric Interaction of *N* Hetons, II: Analysis of the Case of Arbitrary *N*

Konstantin V. Koshel ^{1,2}, Mikhail A. Sokolovskiy ^{3,4,*}, David G. Dritschel ⁵ and Jean N. Reinaud ⁵

¹ Pacific Oceanological Institute of FEB RAS, 43, Baltiyskaya Str., 690041 Vladivostok, Russia; kvkoshel@poi.dvo.ru

² Institute of Applied Mathematics of FEB RAS, 7, Radio Str., 690022 Vladivostok, Russia

³ Water Problems Institute of RAS, 3, Gubkina Str., 119333 Moscow, Russia

⁴ Shirshov Institute of Oceanology of RAS, 36, Nahimovsky Prosp., 117997 Moscow, Russia

⁵ Mathematical Institute, University of St Andrews, St Andrews KY16 9SS, UK; david.dritschel@st-andrews.ac.uk (D.G.D.); jean.reinaud@st-andrews.ac.uk (J.N.R.)

* Correspondence: sokolovskiy@iwp.ru

Abstract: This paper seeks and examines *N*-symmetric vortical solutions of the two-layer geostrophic model for the special case when the vortices (or eddies) have vanishing summed strength (circulation anomaly). This study is an extension [Sokolovskiy et al. *Phys. Fluids* 2020, 32, 09660], where the general formulation for arbitrary *N* was given, but the analysis was only carried out for *N* = 2. Here, families of stationary solutions are obtained and their properties, including asymptotic ones, are investigated in detail. From the point of view of geophysical applications, the results may help interpret the propagation of thermal anomalies in the oceans.

Keywords: vortex dynamics; quasi-geostrophy; point vortex; heton; choreography



Citation: Koshel, K.V.; Sokolovskiy, M.A.; Dritschel, D.G.; Reinaud, J.N. *N*-Symmetric Interaction of *N* Hetons, II: Analysis of the Case of Arbitrary *N*. *Fluids* **2024**, *9*, 122. <https://doi.org/10.3390/fluids9060122>

Academic Editors: Mathieu Sellier and Stéphane Le Dizès

Received: 13 March 2024

Revised: 16 May 2024

Accepted: 21 May 2024

Published: 24 May 2024



Copyright: © 2024 by the authors. Licensee MDPI, Basel, Switzerland. This article is an open access article distributed under the terms and conditions of the Creative Commons Attribution (CC BY) license (<https://creativecommons.org/licenses/by/4.0/>).

1. Introduction

The concept of point-vortex hetons, proposed in [1,2] as the simplest model of vortex heat flow, is based on the equations of geophysical fluid dynamics [3]. It has found a wide range of applications in oceanic [4–20], atmospheric [21–24] and laboratory [25–28] research. Hetons are most effectively used to model the propagation of temperature anomalies and, in particular, to explain the phenomenon of deep convection in the ocean [14–16,29–37]. Although hetons are relatively simple entities, the dynamics of a collection of hetons may exhibit both regular and chaotic motion [2,11,37–43].

The study of finite-core hetons has proved especially fruitful [44,45]. In particular, collections of finite-core hetons in mutual equilibrium have been found, and their stability addressed. Their nonlinear interactions are highly varied, including vortex merger, vortex splitting, filamentation, as well as vertical alignment [42,46–60].

In this paper, we extend the results obtained in [61] (hereafter referred to as SKDR), for both point vortices and finite-core vortices, to the case of an arbitrary *N*. The paper is organised as follows. The formulation of the general problem for the motion of *N* hetons found in SKDR is restated in Section 2. The complete system of $2N$ differential equations is reduced to four equations for an ‘equivalent’ heton, and subsequently to just two equations for a ‘virtual’ heton. Next, in Section 3, the possible modes of behaviour for the heton system, following from the properties of the Hamiltonian, are described. Furthermore, vortex trajectories for various distinct types of motion are presented, and the class of so-called ‘choreographies’ is considered. The interesting problem of the direction of rotation of the vortices located at the vertices of the larger *N*-gon is discussed separately. Section 4 compares the evolution of the point-vortex hetons with the evolution of the more realistic finite-core hetons on selected examples. Section 5 discusses our main findings and their implications, as well as open problems for future research. Appendix A provides

useful formulas for reference. Appendix B contains a detailed analysis of the asymptotic properties of the mean angular velocity of the vortex rotation.

2. Mathematical Model and Problem Formulation

We consider the motion of a system of $2N$ point vortices in a two-layer quasi-geostrophic flow. For simplicity, the layers are taken to have equal non-dimensional thickness $h_1 = h_2 = 1/2$. In the conclusions, we discuss $h_1 \neq h_2$ as a natural extension. Each layer contains N identical vortices, initially located at the vertices of a regular N -gon. Vortices in different layers have opposite strengths (volume-integrated potential vorticity), so that the net integrated potential vorticity is zero. The two regular N -gons have the same centre, but can have different size. Additionally, the two regular N -gons can be offset by an angle (see Figure 1) which shows two examples of initial conditions for $N = 6$.

The equations are simplest if we introduce the complex coordinate $z_j^\alpha = x_j^\alpha + iy_j^\alpha$ for the α^{th} vortex in layer j (with $j = 1$ for the upper layer and $j = 2$ for the lower layer). The vortex strengths κ_j^α are all equal to $\kappa_2^\alpha = \kappa > 0$ in the lower layer and to $\kappa_1^\alpha = -\kappa < 0$ in the upper layer, corresponding to ‘warm’ hetons, following [1].

The vortex motion in an unbounded horizontal domain is governed by the ordinary differential equations [57]

$$\begin{aligned} \dot{z}_j^\alpha = & \frac{(-1)^j \kappa}{4\pi i} \left\{ \sum_{\substack{\beta=1 \\ \beta \neq \alpha}}^N \frac{1}{z_j^\alpha - z_j^\beta} \left[1 + \gamma |z_j^\alpha - z_j^\beta| K_1(\gamma |z_j^\alpha - z_j^\beta|) \right] \right. \\ & \left. - \sum_{\beta=1}^N \frac{1}{z_j^\alpha - z_{3-j}^\beta} \left[1 - \gamma |z_j^\alpha - z_{3-j}^\beta| K_1(\gamma |z_j^\alpha - z_{3-j}^\beta|) \right] \right\}, \end{aligned} \tag{1}$$

where $j = 1, 2$ and $\alpha = 1, 2, \dots, N$. Here, \bar{q} denotes the complex conjugate of any quantity q , while K_1 is the first-order modified Bessel function of the second kind, and $\gamma = 1/\lambda$ is the inverse internal Rossby deformation length $\lambda = \sqrt{g'h_1h_2/(h_1 + h_2)}/f$, with $g' = g\Delta\rho/\rho_0$ being the reduced gravity, g is the acceleration due to gravity, $\Delta\rho = \rho_2 - \rho_1$ (ρ_1 and ρ_2 are the densities of upper and lower layers, respectively, while ρ_0 is the mean density).

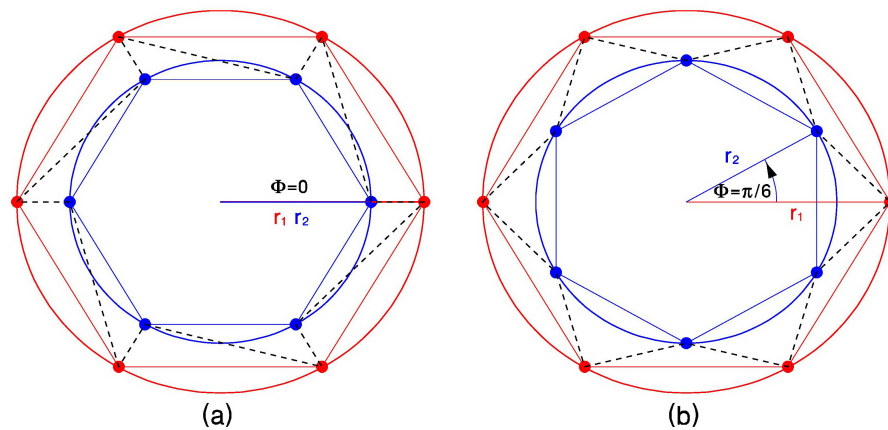


Figure 1. Schematic of the initial vortex system with $r_2 < r_1$ and $N = 6$ (viewed from above): (a) $\Phi = 0$; (b) $\Phi = \pi/6$, where Φ is the angle by which the vortex polygons are offset. The solid lines correspond to polygons with circumscribed radii r_1 and r_2 , and the dashed lines correspond to a polygon with $2N = 12$ sides joining the vortices in both layers. Red (‘warm’) and blue (‘cold’) colours mark the auxiliary lines and vortices in the upper and lower layers, respectively.

Note that Equation (1) is invariant under both translation and rotation. It follows that the two real components, P_x and P_y , of the linear impulse and the angular impulse, M ,

$$P_x + iP_y = \frac{\kappa}{2} \sum_{j=1}^2 (-1)^j \sum_{\alpha=1}^N z_j^\alpha \quad \text{and} \quad M = \frac{\kappa}{2} \sum_{j=1}^2 (-1)^j \sum_{\alpha=1}^N |z_j^\alpha|^2 \tag{2}$$

are invariants of motion. Moreover, the linear impulse is zero in each layer. A further invariant is the Hamiltonian, or interaction energy. It takes the form

$$H = - \frac{\kappa^2}{8\pi} \sum_{j=1}^2 \left\{ \sum_{\substack{\alpha, \beta=1 \\ \alpha \neq \beta}}^N \left[\ln |z_j^\alpha - z_j^\beta| - \text{K}_0 \left(\gamma |z_j^\alpha - z_j^\beta| \right) \right] \right. \\ \left. - \sum_{\alpha, \beta=1}^N \left[\ln |z_{(3-j)}^\alpha - z_j^\beta| + \text{K}_0 \left(\gamma |z_{(3-j)}^\alpha - z_j^\beta| \right) \right] \right\}. \tag{3}$$

Henceforth, we restrict attention to the N -fold symmetric situation. It follows from the invariants (2) that this symmetry is preserved for all time. Moreover, one can find a solution of (1) of the form

$$z_j^\alpha = z_j(t) e^{i \frac{2\pi(\alpha-1)}{N}} = r_j(t) e^{i \left(\varphi_j(t) + \frac{2\pi(\alpha-1)}{N} \right)}, \quad j = 1, 2, \alpha = 1, 2, \dots, N. \tag{4}$$

For the initial configurations described in Figure 1, the initial angles are $\varphi_1(0) = 0$, $\varphi_2(0) = 0$ in panel (a) and $\varphi_1(0) = 0$, $\varphi_2(0) = \pi/N$ in panel (b).

Remark 1. Equation (2) for the angular impulse M simplifies to $(r_1)^2 - (r_2)^2 = -2M/\kappa N$. Since the latter is invariant, it follows that for any motion of the hetons, r_1 and r_2 must always increase or decrease simultaneously and, in particular, take extreme values synchronously. This fact is used in the analysis of the regimes of vortex motion.

Substituting a solution in the form (4) into (1) allows one to obtain evolution equations for the radial r_j and angular coordinates φ_j of an ‘equivalent’ heton (see SKDR). Using angular momentum conservation, we can write the equations for the radial coordinates in the form:

$$\dot{r}_j = \frac{R \varrho^{2-j}}{1 - \varrho^2}; \quad j = 1, 2. \tag{5}$$

Here, $\varrho = \frac{r_2}{r_1}$, $R \equiv r_1$, $R^2 = -\frac{2\tilde{M}}{N(1-\varrho^2)}$ ($\tilde{M} = \frac{M}{\kappa}$), and

$$\dot{\varphi} = -\frac{\kappa(1-\varrho^2)}{4\pi R^2} \left[\gamma R \sum_{n=0}^{N-1} \frac{\sin(\Phi + \frac{2\pi n}{N})}{G(\varrho, \Phi, n)} \text{K}_1(\gamma R G(\varrho, \Phi, n)) \right. \\ \left. - \frac{N\varrho^{N-1} \sin N\Phi}{1 + \varrho^N(\varrho^N - 2 \cos N\Phi)} \right]. \tag{6}$$

The equations for the angular coordinates φ_j have the form

$$\begin{aligned} \dot{\varphi}_1 = & -\frac{\kappa}{4\pi R^2} \left[\gamma R \left(\sum_{n=1}^{N-1} \sin \frac{\pi n}{N} K_1 \left(2\gamma R \sin \frac{\pi n}{N} \right) \right. \right. \\ & + \left. \sum_{n=0}^{N-1} \frac{1 - \varrho \cos \left(\Phi + \frac{2\pi n}{N} \right)}{G(\varrho, \Phi, n)} K_1 \left(\gamma R G(\varrho, \Phi, n) \right) \right) \\ & \left. - \frac{1}{2} \left(\frac{N(1 - \varrho^{2N})}{1 + \varrho^N(\varrho^N - 2 \cos N\Phi)} + 1 \right) \right], \end{aligned} \tag{7}$$

$$\begin{aligned} \dot{\varphi}_2 = & \frac{\kappa}{4\pi R^2 \varrho^2} \left[\gamma R \varrho \left(\sum_{n=1}^{N-1} \sin \frac{\pi n}{N} K_1 \left(2\gamma R \varrho \sin \frac{\pi n}{N} \right) \right. \right. \\ & + \left. \sum_{n=0}^{N-1} \frac{\varrho - \cos \left(\Phi + \frac{2\pi n}{N} \right)}{G(\varrho, \Phi, n)} K_1 \left(\gamma R \varrho G(\varrho, \Phi, n) \right) \right) \\ & \left. + \frac{1}{2} \left(\frac{N(1 - \varrho^{2N})}{1 + \varrho^N(\varrho^N - 2 \cos N\Phi)} - 1 \right) \right], \end{aligned} \tag{8}$$

where $\Phi \equiv \varphi_2 - \varphi_1$. (Note that the argument $\sin \frac{\pi n}{N}$ of K_1 is positive for all $n = 1, 2, \dots, N - 1$). In Equations (7) and (8) above,

$$G(\varrho, \Phi, n) = \sqrt{1 + \varrho \left[\varrho - 2 \cos \left(\Phi + \frac{2\pi n}{N} \right) \right]}. \tag{9}$$

We have thus reduced the original system of $4N$ Equation (1) to a system of just three equations, (5), (7) and (8). The trajectories of the remaining $N - 1$ hetons can be recovered by simple rotations through angles $2\pi n/N$, $n = 1, 2, \dots, N - 1$.

For a general qualitative analysis of this reduced dynamical system, it is convenient to further reduce (5)–(8) to a system of two equations for a ‘virtual’ vortex. The right-hand sides of (5) and (7)–(8) only depend on Φ , the angular difference between the lower-layer and upper-layer vortices (not on φ_1 and φ_2). This fact allows us to reduce the system to just two equations. The first is Equation (6) above for $\varrho = r_2/r_1$, while the second is

$$\begin{aligned} \dot{\Phi} = & \frac{\kappa}{4\pi R^2 \varrho^2} \left\{ \frac{1}{2} \left(\frac{N(1 - \varrho^{2N})(1 - \varrho^2)}{1 + \varrho^N(\varrho^N - 2 \cos N\Phi)} - (1 + \varrho^2) \right) \right. \\ & + \gamma R \varrho \left[\sum_{n=1}^{N-1} \sin \frac{\pi n}{N} \left(\varrho K_1 \left(2\gamma R \sin \frac{\pi n}{N} \right) + K_1 \left(2\gamma R \varrho \sin \frac{\pi n}{N} \right) \right) \right. \\ & \left. \left. - \sum_{n=0}^{N-1} \frac{((1 + \varrho^2) \cos \left(\Phi + \frac{2\pi n}{N} \right) - 2\varrho)}{G(\varrho, \Phi, n)} K_1 \left(\gamma R G(\varrho, \Phi, n) \right) \right] \right\} \end{aligned} \tag{10}$$

for $\Phi = \varphi_2 - \varphi_1$.

The Hamiltonian (3), re-expressed in the variables (ϱ, Φ) , takes the form

$$\begin{aligned} H = & \frac{\kappa^2}{4\pi} \left[\ln \frac{R^2(1 + \varrho^N(\varrho^N - 2 \cos N\Phi))}{\varrho^{N-1}} + 2 \sum_{n=0}^{N-1} K_0(\gamma R G(\varrho, \Phi, n)) \right. \\ & \left. + \sum_{n=1}^{N-1} \left(K_0 \left(2\gamma R \sin \frac{\pi n}{N} \right) + K_0 \left(2\gamma R \varrho \sin \frac{\pi n}{N} \right) \right) \right]. \end{aligned} \tag{11}$$

Here, we have used the properties of trigonometric products, see Equation (A2) of Appendix A. It is convenient to re-express Equations (6) and (10) in their Hamiltonian form

$$\dot{\varrho} = \frac{1 - \varrho^2}{2\kappa\varrho R^2} \frac{\partial H}{\partial \Phi}, \quad \dot{\Phi} = -\frac{1 - \varrho^2}{2\kappa\varrho R^2} \frac{\partial H}{\partial \varrho}, \tag{12}$$

explicitly showing this is a (reduced) Hamiltonian system.

3. Analysis of Possible Motion Regimes

The possible motion regimes are completely determined by the structure of the Hamiltonian. The phase portrait of the Hamiltonian $H(\varrho, \Phi)$ is shown in Figure 2 for $\tilde{M} = -1.2$ and $N = 2, 3$ and 4. The interval $\Phi \in [0; 2\pi]$ includes the entire periodically repeating structure of heton system.

Separatrices delimit regions of localised and unbounded motions. The intersections of the separatrices (red dashed lines) at the hyperbolic points occur at values of ϱ , for which the two vortex N -gons are in relative equilibrium for $\Phi = \pi/N$. Such a case is shown in Figure 1b for $N = 6$. Scanning across in ϱ for any fixed Φ , bounded or localised motions occur only between the separatrices.

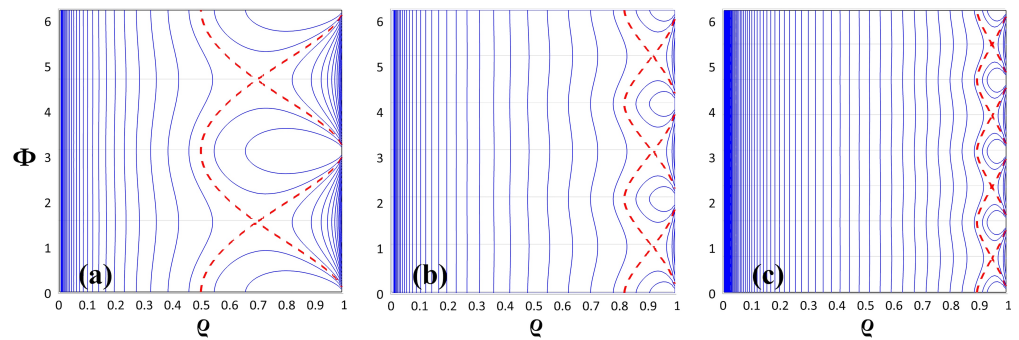


Figure 2. Examples of Hamiltonian phase portraits $H(\varrho, \Phi)$ for $\varrho \in [0; 1]$ and $\Phi \in [0; 2\pi]$, at $\tilde{M} = -1.2$: (a) $N = 2$; (b) $N = 3$; (c) $N = 4$. The thin horizontal lines in each panel indicate $\Phi = n\pi/N$ ($n = 0, 1, \dots, 2N$). The red dashed lines are the separatrices of field $\Phi(\varrho)|_{\tilde{M}=-1.2}$, delimiting regions of localised and unbounded motions.

It should be noted that the system is invariant through a rotation of $\frac{2\pi}{N}$, so it suffices to consider the values $\Phi = 0$ and $\Phi = \frac{\pi}{N}$ for the virtual vortex. In both cases, the equalities $(\dots)_i = -(\dots)_{N-i}$ hold, where (\dots) are the expressions within the sums (see Appendix A). It follows that the right-hand side of (6) vanishes for these values of Φ , and ϱ reaches an extremum. This means that

$$\dot{\varrho}(\Phi = 0, \frac{\pi}{N}) = 0, \tag{13}$$

which is clearly seen in Figure 2. The same is true for $r_{1,2}$ due to Equation (5).

To analyse the extrema,

$$\varrho^- = \varrho(\Phi = 0), \quad \varrho^+ = \varrho(\Phi = \frac{\pi}{N}) \tag{14}$$

we evaluate the second derivative of ϱ ,

$$\ddot{\varrho}|_{\Phi=0, \frac{\pi}{N}} = \frac{1 - \varrho^2}{2\kappa\varrho R^2} \frac{\partial^2 H}{\partial \Phi^2} \dot{\Phi}|_{\Phi=0, \frac{\pi}{N}}. \tag{15}$$

It is shown in Appendix B that $\frac{\partial^2 H}{\partial \Phi^2} > 0$ and $\dot{\Phi} > 0$ for $\Phi = 0$. Hence, the extremum ϱ^- is always a minimum. It is also shown that $\frac{\partial^2 H}{\partial \Phi^2} < 0$ for $\Phi = \pi/N$. However, $\dot{\Phi}$ changes sign in this case. We have $\dot{\Phi} > 0$ for $\varrho^+ < \varrho^*$, $\dot{\Phi} = 0$ at $\varrho^+ = \varrho^*$ and $\dot{\Phi} < 0$ for $\varrho^+ > \varrho^*$.

This means that, for $0 \leq \varrho^+ < \varrho^*$, the second derivative $\ddot{\varrho}^+ < 0$ and ϱ^+ is maximum on this interval. Then, the second derivative $\ddot{\varrho}^+ > 0$ for $\varrho^* < \varrho^+ < 1$ and ϱ^+ is minimum on this interval.

The extreme values of ϱ can be obtained from the equation

$$H(\Phi^\pm, \varrho^\pm) = \bar{H}, \quad \Phi^- = 0, \quad \Phi^+ = \frac{\pi}{N}, \tag{16}$$

where \bar{H} is a some fixed value of the Hamiltonian. It is, therefore, useful to analyse, in turn, the extreme values of the Hamiltonian (see also [61–63]):

$$H^- = H(\Phi^-, \varrho^-), \quad H^+ = H(\Phi^+, \varrho^+). \tag{17}$$

To this end, we examine the dependence of H^- and H^+ on ϱ^\pm in Figure 3. Here, we restrict attention to the interval $0 < \varrho < 1$ without loss of generality, since the situation $\varrho > 1$ corresponds to swapping the two layers. It is shown in Appendix B that both H^- and H^+ tend to infinity as $\varrho \rightarrow 0$, due to a logarithmic singularity.

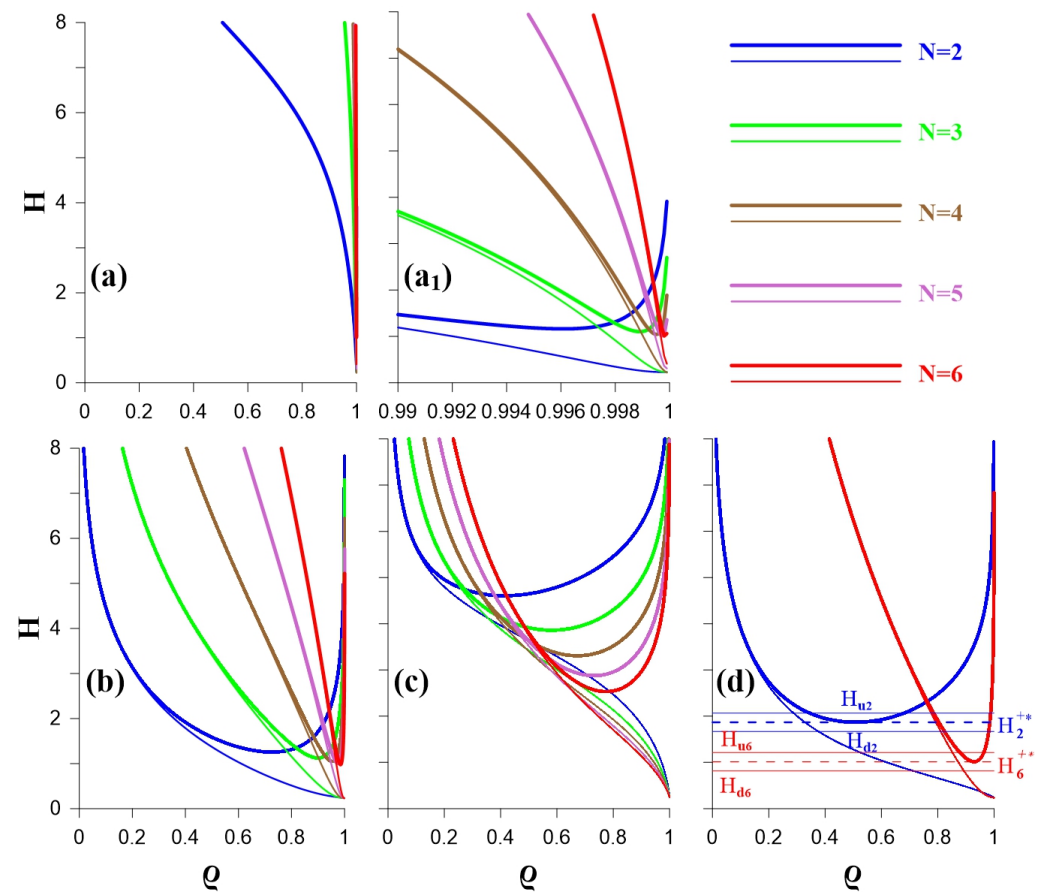


Figure 3. H^+ (thick lines) and H^- (thin lines) as a functions of ϱ for $N = 2, 3, 4, 5, 6$: (a) $\tilde{M} = -0.001$; (a₁) the same as (a), but on the interval $\varrho \in [0.99; 1.00]$, i.e., the horizontal axis is scaled by a factor 100; (b) $\tilde{M} = -1$; (c) $\tilde{M} = -100$. In panel (d), $\tilde{M} = -5$ is shown only for $N = 2$ and 6. The dashed horizontal line shows the minimum values of H^+ , denoted H_2^{+*} and H_6^{+*} , found at $\varrho = \varrho_2^{+*}$ and $\varrho = \varrho_6^{+*}$ respectively. (Here, $H_2^{+*} \approx 1.8680$ at $\varrho_2^{+*} = 0.5078$ and $H_6^{+*} \approx 1.0135$ at $\varrho_6^{+*} = 0.9296$.) Two additional lines of constant energy are drawn in solid: $H = H_{u_2}$ lying above H_2^{+*} , and $H = H_{d_2}$ lying below H_2^{+*} for $N = 2$ (blue horizontal lines); also, $H = H_{u_6}$ and $H = H_{d_6}$ for $N = 6$ (red horizontal lines). The intersections of either of these lines with $H^-(\varrho)$ are denoted by ϱ_2^- and ϱ_6^- , respectively. Note, the lines $H = H_{u_2}$ and $H = H_{u_6}$ intersect the curves H^+ at two points, which we denote $\varrho = \varrho_2^{+1}$ and ϱ_2^{+2} when $N = 2$, and $\varrho = \varrho_6^{+1}$ and ϱ_6^{+2} when $N = 6$. Note that $\varrho_N^{+2} > \varrho_N^{+1}$.

For $q \rightarrow 1$, the situation differs. H^+ tends to infinity (see (A24)), but H^- tends to a finite constant (see (A25)). Since $\frac{\partial H^-}{\partial q}$ is always negative (see Section 3) one concludes that this derivative is a monotonically decreasing function of q . On the other hand, $\frac{\partial H^+}{\partial q}$ changes sign at $q = q^*$, as shown in Appendix B. Thus, H^+ has a minimum at $q = q^*$.

It is also shown in Appendix B that the difference $H^+ - H^-$ is always positive, but remains very small for small q^+ and q^- . The amplitude of the oscillation $q^+ - q^-$ is also very small for $q \ll q^*$.

We next analyse the influence of the angular momentum and the number of vortices N on H^- and H^+ . We examine the possible localised (periodic) and non-localised (unbounded) types of motion. For this, it is convenient to introduce the following definitions, which are depicted graphically in Figure 3. We define q^* as the value of q , for which the function H^+ has a minimum H^{+*} (the dashed horizontal lines in Figure 3d). We also define q^- to be the intersection point between $H^-(q)$ and either of the two levels of constant energy, $H = H_d$ or H_u , are defined so that $H_d < H^{+*}$ and $H_u > H^{+*}$. Finally, we define q^{+1} and q^{+2} to be the minimum and the maximum solutions to $H^+(q) = \mathcal{H}_u$.

It is shown in Appendix B that q^- and q^{+2} always correspond to minima of q , while q^{+1} always corresponds to a maximum of q , for a given energy $H = \bar{H}$. It is worth mentioning that the limit $q \rightarrow 1$ corresponds to the limit $r_1, r_2 \rightarrow \infty$. If $q = 1$ at $t = 0$, it follows from (12) that $q = 1$ for all times since $\dot{q} = 0$ exactly. For this special case, Equation (10) simplifies to

$$\begin{aligned} \dot{\Phi} &= \frac{\kappa}{4\pi R^2} \sum_{n=1}^{N-1} \sin \frac{\pi n}{N} K_1 \left(2\gamma R \sin \frac{\pi n}{N} \right) \\ &+ 2\gamma R \sum_{n=0}^{N-1} \left| \sin \left(\frac{\Phi}{2} + \frac{\pi n}{N} \right) \right| K_1 \left(2\gamma R \left| \sin \left(\frac{\Phi}{2} + \frac{\pi n}{N} \right) \right| \right) - 1, \end{aligned} \tag{18}$$

where $R = r_1 = r_2$. This special case was studied in [1] (see also [11,38,57]). It was shown that there exists $R = R^*$ such that the solutions to (18) are localised and periodic, and the corresponding trajectories follow closed quasi-quadrangular patterns for $R < R^*$. The trajectories are unbounded for $R > R^*$. Thus, one deduces three possible regimes of motion (see also Figure 3 for illustration) for the virtual vortex:

- (A) Unbounded motion within the interval $q^- \leq q \leq 1$, when $H < H^{+*}$;
- (B) Localised (bounded and periodic) motion within the interval $q^- \leq q \leq q^{+1}$, when $H > H^{+*}$;
- (C) Unbounded motion within the interval $q^{+2} \leq q \leq 1$, when $H > H^{+*}$.

For example, if we initialise the system with $q(0) = q_0 = q^+$ and $\Phi(0) = \Phi_0 = \pi/N$, and choose a value of the angular momentum \tilde{M} to determine the initial values of the radial coordinates r_{10} and r_{20} , the subsequent motion will be localised (bounded) if $q^+ < q^*$, but unbounded if $q^+ > q^*$. Both cases, in fact, correspond to the same condition: $H > H^{+*}$. It is worth mentioning that it is impossible to have $H < H^{+*}$ for $q(0) = q_0 = q^+$ and $\Phi(0) = \Phi_0 = \pi/N$, irrespective of \tilde{M} . We consider the case $H < H^{+*}$ separately below.

The region of unbounded motions $[\infty]$ is shaded in blue in Figure 4. The critical curve $\tilde{M}(q^*)$ separating bounded and unbounded motion is found by solving the equation

$$\frac{\partial H^+}{\partial q} = \frac{\partial H(\Phi = \frac{\pi}{N}, q)}{\partial q} = 0 \tag{19}$$

for each value of \tilde{M} . Notably, the asymptotes of this critical curve can be found for large values of $-\tilde{M}$, see Appendix B. We find

$$q^* = 1 - \frac{\delta^*}{N}, \quad R^* \approx \sqrt{-\frac{\tilde{M}}{\delta^*}} \quad (\delta^* \approx 1.5485, -\tilde{M} \gg 1) \tag{20}$$

and the asymptotes are indicated in Figure 4a–c by the vertical dashed lines; the boundary of the $[\infty]$ regions approaches the respective asymptotes as $-M \rightarrow \infty$.

An approximate form of the boundary of the region of parameter space corresponding to unbounded motion can also be found from Equation (A16) in Appendix B:

$$-\tilde{M} \approx 0.827 \frac{N^3}{\gamma^2 \pi^2} (1 - \varrho^2) \tag{21}$$

for small $(1 - \varrho)$. For sufficiently large N and $\gamma RG(\varrho, \Phi, n) \geq 1$, the value of δ^* in Equation (20) can be determined from Equation (A11) in Appendix B, and we have $\delta^* \sim 1.5485$. For $\gamma RG(\varrho, \Phi, n) \leq 1$ the value of δ^* is smaller. It follows that ϱ^* tends to the right boundary of the region when N grows and when $-\tilde{M}$ decreases. For $2 < N < 10$, we have checked this tendency by direct calculation. This tendency is also shown in Figure 3.

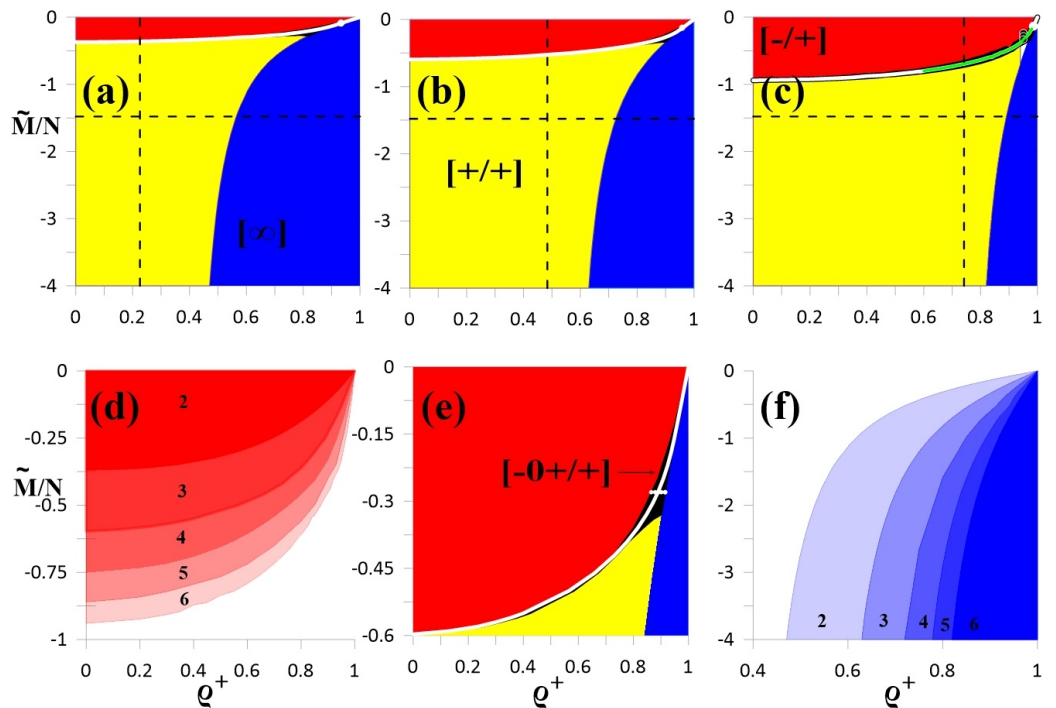


Figure 4. (a–c) Regime diagrams showing the possible types of motion in the $(\varrho^+, \tilde{M}/N)$ -plane, for the initial value $\Phi_0 = \pi/N$ for $N = 2, 3$ and 6 , respectively. The blue $[\infty]$ region corresponds to unbounded motion, while the red $[-/+]$, black $[-0 / +]$ and yellow $[+ / +]$ regions correspond to localised, bounded motions in which all vortices in both layers move within annular zones bounded by concentric circles. The white lines inside the black regions in these panels and in panel (e) correspond to a families of periodic solutions, the so-called ‘absolute choreographies’. The white markers on these lines correspond to parameters used to generate the blue, green and red lines in Figure 6. The black markers in the upper right corner of the panel (c) correspond to the numerical experiments in Figure 8. The green segment on the white line in panel (c) over the interval $\varrho^+ \in [0.60; 0.98]$ corresponds to a family of absolute choreographies shown in Figure 7 below. Horizontal dashed lines are the asymptotes to which the lower boundary of the red region $[- / +]$ approaches at $N \rightarrow \infty$ (see Equation (26)). Vertical lines are asymptotes for the left border of the blue area $[\infty]$ as $\tilde{M} \rightarrow -\infty$ for each N (see Equation (20)). Panel (d) shows regions for the single regime $[- / +]$, for $N = 2, 3, 4, 5$ and 6 (filled with different shades of red). Here, the vertical scale is multiplied by ≈ 5.4 for clarity. Panel (e) shows the case $N = 3$ (as in panel (b)), but with the vertical scale multiplied by 8. Here, the white markers at $\tilde{M}/N = -0.28$ correspond to parameters for the numerical experiments presented in Figure 5. Panel (f) shows regions for the single regime $[\infty]$, for $N = 2, 3, 4, 5$ and 6 (filled with different shades of blue).

Hence, the boundary of the $[\infty]$ -region tends to the point $(\tilde{M}, \varrho) = (0, 1)$ along the curve (21), with a slope increasing with N .

3.1. Examples of Trajectories: Absolute and Relative Choreographies

Panels (a–f) of Figure 5 show early-time trajectories of the equivalent heton for $\tilde{M}/N = -0.28$, $N = 3$, $\Phi(0) = \Phi_0 = \pi/3$ and $\varrho^+ = 0.864, 0.878, 0.8892, 0.9, 0.9144$ and 0.9145 . The parameter values $(\varrho^+, \tilde{M}/N)$ are indicated by white markers in Figure 4e. When $(\varrho^+, \tilde{M}/N) = (0.864, -0.28)$, as shown on Figure 5a, the initial conditions belong to the red region of Figure 4e. This region, symbolised by $[-/+]$, corresponds to cases where the average angular velocity of the orbital motion of the upper layer vortex is negative, and the lower layer vortex is positive. In the general case, in addition to circular motion, the vortices also perform nutational oscillations relative to their mean position. Thus, their trajectories over long times fill concentric annular regions.

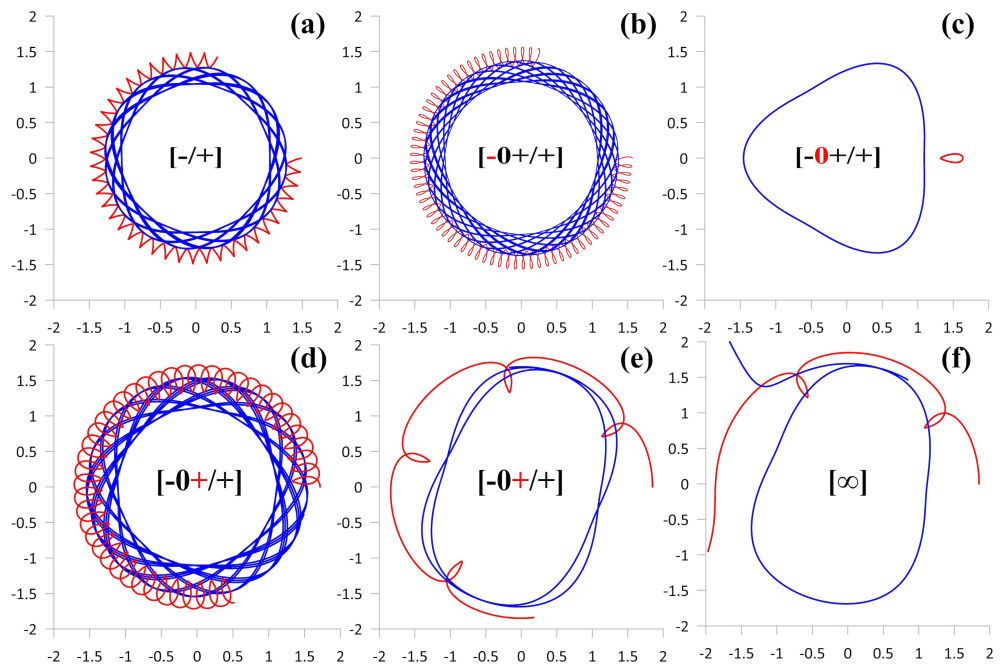


Figure 5. Trajectories of vortices (here and everywhere below, the absolute and relative trajectories of the vortices are depicted in the Cartesian coordinate system (x, y) , the dimensionless horizontal and vertical axis, correspondingly) of the equivalent heton (top view) at early times for $\tilde{M}/N = -0.28$ and $N = 3$: (a) $\varrho^+ = 0.864$; (b) $\varrho^+ = 0.878$; (c) $\varrho^+ = 0.8892$; (d) $\varrho^+ = 0.900$; (e) $\varrho^+ = 0.9144$; (f) $\varrho^+ = 0.9145$. The red lines correspond to the upper-layer vortices, and the blue lines correspond to the lower-layer vortices. Legends in brackets indicate the type of motion (see Figure 4); the symbol corresponding to a specific type of trajectory is highlighted in red in panels (b–e). These experiments are for parameters represented by the white markers for $\tilde{M}/N = -0.28$ in Figure 4e.

Panels (b–e) show examples of motions in the $[-0+ / +]$ region (black area of Figure 4). Symbols ‘-’, ‘0’ and ‘+’, respectively, correspond to an anticyclonic displacement, the absence of any average displacement, and a cyclonic displacement of the upper layer vortex. The symbol ‘+’ after the forward slash corresponds to a cyclonic rotation in lower layer. In each panel of Figure 5, the corresponding symbol is highlighted in red. A characteristic feature of this class of motions is that the sign of the total angular velocity (not averaged) of the upper-layer vortices alternates (nutational trajectories are loop-shaped). In panel (c), the outer vortex only performs periodic nutational motions, while the inner vortex periodically rotates along a fixed quasi-triangular curve (the corresponding marker in Figure 4a lies on the white line). In reality, we have a six-vortex structure, in which three peripheral vortices in the upper layer rotate along individual closed trajectories shifted relative to each other by an angle $\pi/3$, and three vortices in the lower layer move along a common central

quasi-triangular trajectory one after the other with the same angular displacement. For this reason, the trajectories in panel (c) are called ‘absolute complex choreographies’.

Remark 2. Simó [64] introduced the concept of choreography applied to rigid body dynamics. Choreographies can be (a) absolute, if the trajectories are closed in a fixed coordinate system; (b) relative, if the trajectories are closed in a uniformly rotating or translating coordinate system; (c) simple, if all of the material points move along a common trajectory; and (d) complex, if at least one of the points moves along a separate trajectory. The concept of choreography in vortex theory was used for the first time in [65]. Modern studies of choreography as applied to 2D vortex dynamics are presented in [65–69], and for a two-layer rotating fluid in [56,57,61].

It should be noted that the values of the values of the parameter ϱ^+ in panels (b–d) differ only slightly and, therefore, the markers in Figure 4e are almost undistinguishable. The last pair of trajectories of this type in Figure 4e corresponds to initial conditions close to the border of the black region. There, the loops almost disappear, and the trajectory of the outer vortex approaches a circular form. An increase in ϱ^+ by just 0.0001 shifts the initial conditions into the region of unbounded motions, when three two-layer pairs (hetons) scatter in different directions—see Figure 5f. It should be noted that the example of absolute choreographies, shown in Figure 5c, is not unique. Trajectories of this type correspond to points belonging to the white lines in Figure 4a–c,e. The case $N = 2$ was studied in detail in SKDR.

Figure 6 shows a gallery of absolute choreographies for $2 \leq N \leq 6$, corresponding to the maximum values of ϱ^+ (the closed curves or orbits were obtained numerically). We call these periodic trajectories the ‘limiting’ ones. The parameters ϱ^+ and \tilde{M}/N for the cases $N = 2, 3$ and 6 correspond to the white markers in the upper right corners of Figure 4a–c.

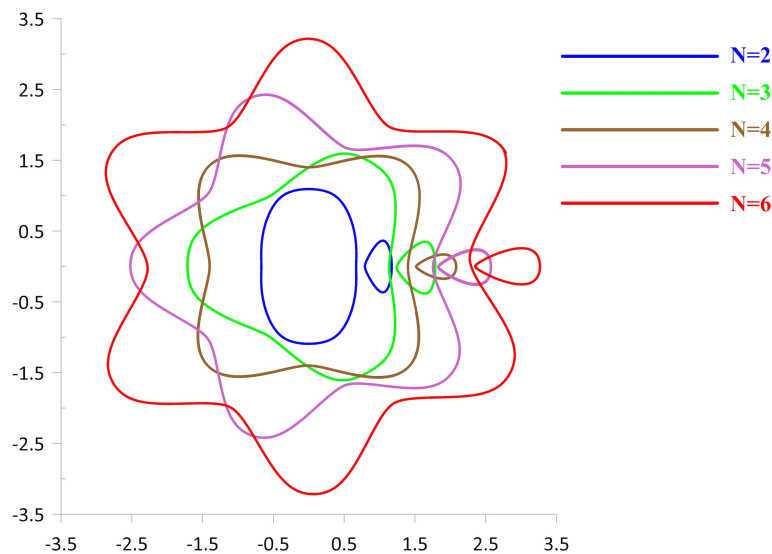


Figure 6. Gallery of the ‘limiting’ periodic trajectories (absolute choreographies) of vortices of an equivalent heton for the following external parameter values $(\varrho^+, \tilde{M}/N)$: (0.9323; -0.0899) for $N = 2$; (0.9543; -0.1223) for $N = 3$; (0.9739; -0.1163) for $N = 4$; (0.9794; -0.1138) for $N = 5$ and (0.9854; -0.1326) for $N = 6$.

Figure 6 shows that the size of internal N -shaped (N -gons with smoothed corners) choreographies increase with increasing of N .

We next consider the topological properties of the choreographies for the case $N = 6$ ($\Phi(0) = \Phi_0 = \pi/6$) in more detail in Figure 7. We show a family of choreographies over an interval for $\varrho^+ \in [0.60; 0.97]$ with an increment of 0.01. This interval is the green portion of the white line in Figure 4c. Numerical experiments show that as ϱ^+ decreases, the quasi-hexagonal choreographies decrease in size in the lower layer and the trajectories

become nearly circular. In the upper layer, the situation is more complicated. For $\varrho^+ \geq 0.97$, the vortices move along thin drop-shaped trajectories, whose innermost tips point towards the origin. For $\varrho^+ = 0.96$, figure-of-eight orbits begin to form due to the emergence of a second closed loop to the left of the tip. Such doubly connected patterns occur in the interval $\varrho^+ \in [0.93, 0.96]$. In this interval, as ϱ^+ decreases, the left part of the ‘eight’ grows, while the right part shrinks. Finally, for $\varrho^+ = 0.93$, the right part completely disappears, and now the drop-shaped trajectory has a tip pointing away from the origin. As we decrease ϱ^+ further, the size of the drop first increases to reach a local maximum at $\varrho^+ \approx 0.90$, and then decreases, eventually shrinking to a point.

We next consider the evolution of the system close to the figure-of-eight stationary states for $\varrho^+ = 0.95$ (purple curves in Figure 7) and for $\varrho^+ = 0.97$ (black curves). The next three figures are devoted to $\varrho^+ = 0.95$, followed by another devoted to $\varrho^+ = 0.97$.

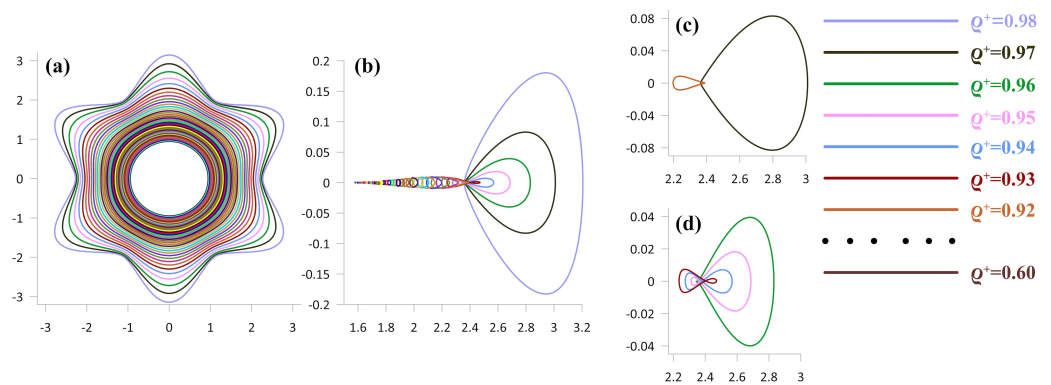


Figure 7. (a,b): Gallery of ‘absolute choreographies’ of the equivalent heton for $N = 6$ ($\Phi(0) = \Phi_0 = \pi/6$) along the interval $\varrho^+ \in [0.60; 0.98]$ with increment 0.01. Each value of ϱ^+ has its own colour, and is the same for the trajectories of the upper and lower layers. Panel (a) shows the lower-layer trajectories in natural scale. Panel (b) shows the upper-layer trajectories in stretched coordinates: 4 times in x and 16 times in y . Panel (c) shows the limiting simply connected upper-layer trajectories at $\varrho^+ = 0.92$ (left) and $\varrho^+ = 0.97$ (right); here, the x scale is expanded by 8 and the y scale is expanded by 40. Panel (d) shows a family of intermediate doubly connected figure-of-eight trajectories for $\varrho^+ = 0.93, 0.94, 0.95$ and 0.96 . The x scale is the same as in panel (c), but the y scale is doubled.

Figure 8 shows a series of vortex trajectories in the vicinity of an equivalent heton with $N = 6$ and $\varrho^+ = 0.95$. Panel (b) shows the absolute choreography of the $[-0+ / +]$ type, for which the vortex trajectory of the upper layer has a figure-of-eight shape, and panels (a) and (c) show the absolute vortex trajectories of types $[-0+ / +]$ and $[-0+ / +]$, respectively, when the upper layer vortex moves along a loop-like trajectory, unwinding in the anticyclonic and cyclonic directions, respectively. This behaviour is found in the black region of Figure 4c.

We construct the relative choreographies for these cases in Figure 8(a₁,c₁). The relative choreographies are the closed trajectories obtained in a reference frame rotating with the average angular velocity ω of the vortex in the upper layer. One may see that the relative choreographies have loop-like absolute upper-layer trajectories (found inside the black region of Figure 4c) also belong to a type of figure-of-eight trajectory. The figure-of-eight relative choreographies also occur in some parts of the red and yellow areas of the diagram, where the upper-layer vortices move along zigzag trajectories—see Figure 9.

Further away from the stationary state, it is possible to obtain drop-shaped relative choreographies, both in the red region (for $\tilde{M}/N = -0.2$) and in the yellow region (for $\tilde{M}/N = -0.5$) in Figure 4c, as shown in Figure 10.

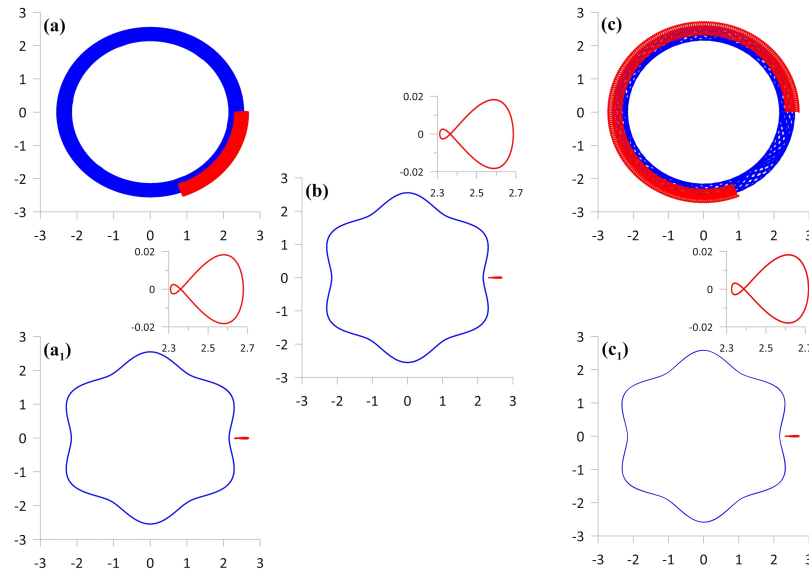


Figure 8. The trajectories of vortices of the equivalent heton (top view) at $q^+ = 0.95$ and $N = 6$: (a) $\bar{M}/N = -0.35$; (b) $\bar{M}/N = -0.35183$ (absolute choreography); (c) $\bar{M}/N = -0.36$. Relative choreographies in panels (a₁,c₁) into which trajectories from panels (a,c) are subject to external rotation with positive and negative angular velocity, respectively. The insets to the right of the choreographies show zooms of the upper-layer closed trajectories (here, x is expanded by 5 and y is expanded by 25).

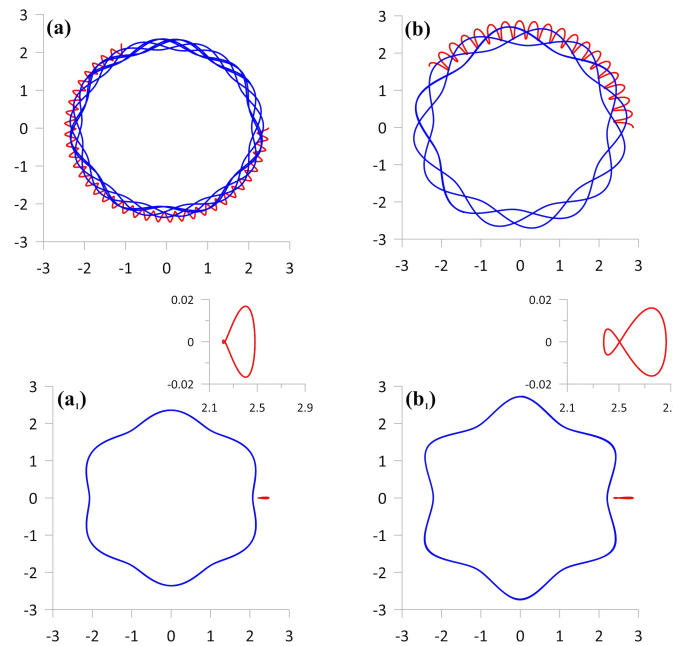


Figure 9. (a,b): Absolute vortex trajectories of an equivalent heton for $N = 6$, $q^+ = 0.95$; (a) $\bar{M}/N = -0.3$ and (b) $\bar{M}/N = -0.4$. Panels (a₁,b₁) show their respective figure-of-eight relative choreographies, into which trajectories from panels (a,b) are subject to external rotation with positive and negative angular velocity, respectively. In the insets, x is expanded by 5 and y is expanded by 25.

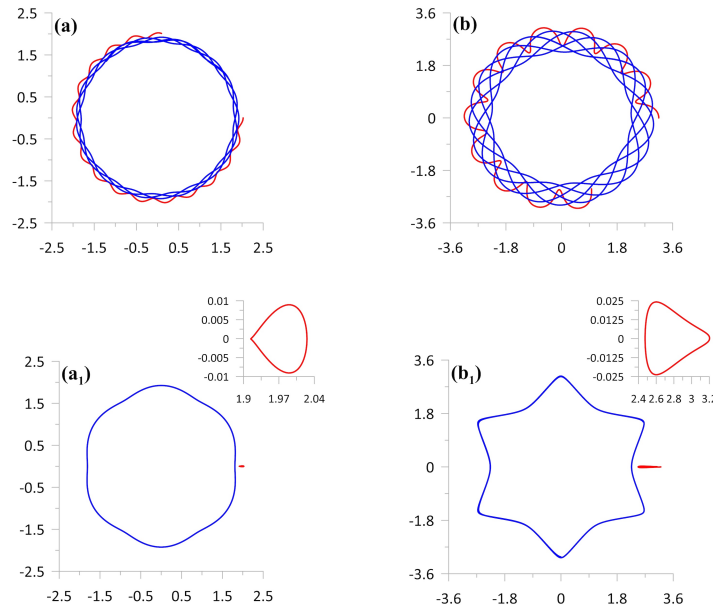


Figure 10. The same as in Figure 9, but for $\tilde{M}/N = -0.2$ (a) and $\tilde{M}/N = -0.5$ (b). Drop-shaped relative choreographies, into which trajectories from panels (a,b) are subject to external rotation with positive and negative angular velocity and are shown in panels (a₁,b₁), respectively. In inset (a₁), x is expanded by 24 and y by 125; in inset (b₁), x is expanded by 9 and y by 72.

We next consider the second class of motions in the vicinity of the stationary state, when the absolute choreography for the vortex of the upper layer has a drop-like shape, i.e., for $q^+ = 0.97$. Results are presented in Figure 11, where all absolute trajectories of the upper-layer vortices are loop-shaped. The initial conditions are in the black region of Figure 4c, outside the yellow [+ / +]-region. All relative choreographies are drop-shaped.

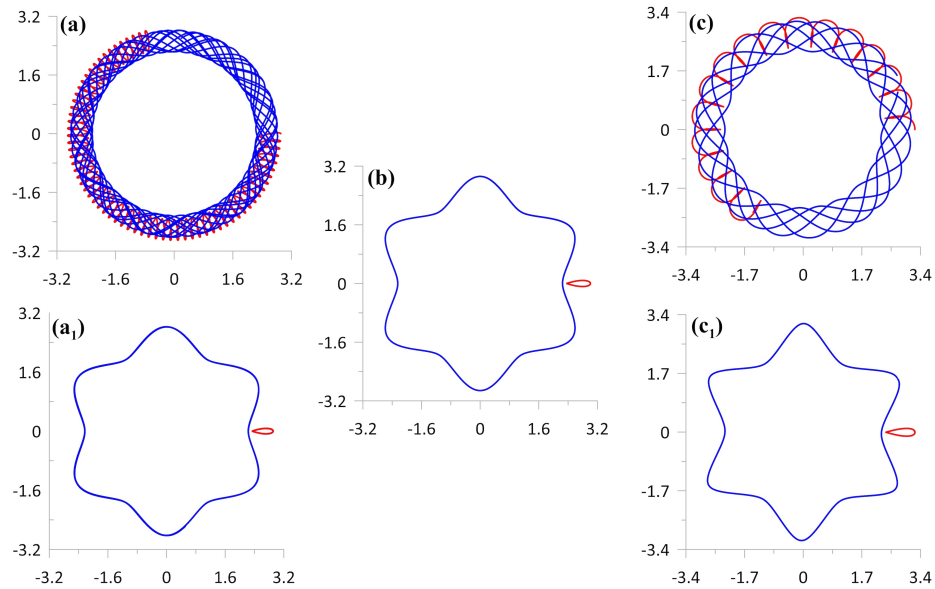


Figure 11. The trajectories of vortices of the equivalent heton (top view) at $q^+ = 0.97$ and $N = 6$: (a) $\tilde{M}/N = -0.25$ (type [-0+ / +]); (b) $\tilde{M}/N = -0.26767$ (absolute choreography, type [-0+ / +]); (c) $\tilde{M}/N = -0.31$ (type [-0+ / +]). Relative choreographies in panels (a₁,c₁), into which trajectories from panels (a,c) are subject to external rotation with positive and negative angular velocity, respectively.

Let us point out another new type of absolute choreography in the N -symmetric dynamics of N hetons. In this choreography, trajectories are circular synchronous rotations

of the lower-layer and upper-layer vortices around a common centre. Clearly, these movements are of the [+ / +] type (the yellow areas in Figure 4). For a circular motion, the right-hand side of Equation (5) must be zero, i.e., $q \equiv 0$, and we must have $\omega_1 = \dot{\phi}_1 = \omega_2 = \dot{\phi}_2$ (see Equations (7) and (8)). These conditions are satisfied for a discrete set of parameters in the plane $(q^+, \tilde{M}/N)$ in a narrow neighbourhood of the yellow region near the boundary of the region $[\infty]$. Two examples of such circular choreographies for $N = 5$ and 6 are shown in Figure 12. Markers in the figure only show the initial location of the two vortices of the equivalent heton. In reality, five (respectively, six) anticyclones/cyclones in the upper/lower layer move counter-clockwise, with the same angular velocity, thereby preserving the regular pentagonal or hexagonal shape.

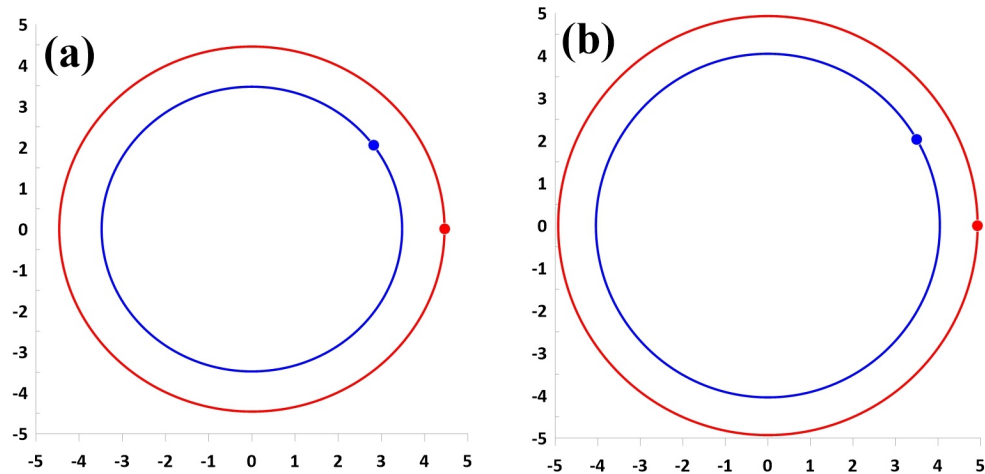


Figure 12. The circle choreographies for (a): $N = 5$ ($\Phi = \pi/5$), $q^+ = 0.78$, $\tilde{M}/N = -3.8923$, $r_1 = 4.4598$, $r_2 = 3.4787$ and (b): $N = 6$ ($\Phi = \pi/6$), $q^+ = 0.82$, $\tilde{M}/N = -3.9796$, $r_1 = 4.4930$, $r_2 = 4.0427$. Markers indicate the initial position of the equivalent heton vortices.

3.2. Direction of Rotation of the External Vortices

Since we assume throughout that $r_1 > r_2$ (as in Figure 1), the external N -gon is in the upper layer. Thus, ‘external/internal’ and ‘upper-layer/lower-layer’ are synonymous in this context. The internal vortices always maintain their direction of rotation, while the external ones can change it.

The direction of rotation of the external vortices depends on the region of the parameter space. The external vortices are expected to rotate in the opposite (anticyclonic) direction if the interaction between the two layers is sufficiently weak. In the parameter space (q^+, \tilde{M}) in Figure 4, this anticyclonic motion occurs in the red $[- / +]$ region. To determine the boundary of this region, we determine the value of the angular impulse $\tilde{M}(q^+)$ at which the angular velocity of the external vortices vanishes. This leads to the implicit equation:

$$\begin{aligned} \dot{\phi}_1^+ &= \frac{\kappa}{4\pi R^2} \left[\frac{N(1 - q^N) + 1 + q^N}{2(1 + q^N)} - \sum_{n=1}^{N-1} \gamma R \sin \frac{\pi n}{N} K_1 \left(2\gamma R \sin \frac{\pi n}{N} \right) \right. \\ &\quad \left. - \sum_{n=0}^{N-1} \frac{1 - q \cos \frac{\pi(1+2n)}{N}}{G(q, \frac{\pi}{N}, n)} \gamma R K_1 \left(\gamma R G(q, \frac{\pi}{N}, n) \right) \right] = 0. \end{aligned} \tag{22}$$

Analytical progress can be made assuming $q \ll 1$. Then, Equation (22) reduces to

$$\dot{\phi}_1^+ = \frac{\kappa}{4\pi R^2} \left[\frac{N + 1}{2} - \frac{1}{2} \sum_{n=1}^{N-1} 2\gamma R \sin \frac{\pi n}{N} K_1 \left(2\gamma R \sin \frac{\pi n}{N} \right) - N\gamma R K_1(\gamma R) \right] = 0. \tag{23}$$

We can estimate the solution by manipulating the sum in the equation. On the one hand, if we neglect the sum, we obtain the approximate value of $R = 1.257$, which is smaller

than the actual solution to Equation (23). On the other hand, we can find an upper bound for the sum in question:

$$\begin{aligned} & \sum_{j=1}^{N-1} \sum_{n=n_j}^{n_{j+1}} 2\gamma R \sin \frac{\pi n}{N} K_1 \left(2\gamma R \sin \frac{\pi n}{N} \right) \\ < & \sum_{j=1}^{N-1} (n_{j+1} - n_j) 2\gamma R \sin \frac{\pi n_j}{N} K_1 \left(2\gamma R \sin \frac{\pi n_j}{N} \right), \quad n_1 = 0, n_2 = 1, \dots, n_N = N - 1, \end{aligned} \quad (24)$$

from which we obtain the upper bound $R = 2$ for the solution to (23). Thus, we obtain the following bounds for the solution:

$$1.257 < \gamma R(\varrho^+ = 0) = \gamma \sqrt{\frac{-2\tilde{M}}{N}} < 2, \quad \tilde{M} = -\frac{N}{2} R^2(\varrho^+ = 0). \quad (25)$$

Numerical solutions to Equation (23) for $50 \leq N \leq 100$ suggest that $R(\varrho^+ = 0)$ tends to $R_0^\infty \approx 1.72$.

From this result, we conclude that the boundary of the $[-/+]$ region corresponds to

$$\tilde{M} = -\frac{N}{2} (R_0^\infty)^2 \approx -1.4792N, \quad (26)$$

when $\varrho \rightarrow 0$, and decreases with N . The limiting lower boundary $\tilde{M}/N \approx -1.4792$ of the red regions is shown in Figure 4a–c by the dashed horizontal lines.

We next consider the direction of rotation of the internal (lower-layer) vortices. Their angular velocity at the minimum of $r_2 = R\varrho$ is found from

$$\begin{aligned} \phi_2^- &= \frac{\kappa}{4\pi R^2 \varrho^2} \left[\sum_{n=1}^{N-1} \gamma R \varrho \sin \frac{\pi n}{N} K_1 \left(2\gamma R \varrho \sin \frac{\pi n}{N} \right) \right. \\ &+ \left. \gamma R \varrho \sum_{n=0}^{N-1} \frac{\varrho - \cos \frac{2\pi n}{N}}{G(\varrho, 0, n)} K_1(\gamma R G(\varrho, 0, n)) + \frac{N - 1 + (N + 1)\varrho^N}{2(1 - \varrho^N)} \right]. \end{aligned} \quad (27)$$

We can see that ϕ_2^- is always positive. In Equation (27), only the second sum can be negative, but at sufficiently large R this sum is exponentially small. For small R one can use (A6) and approximate K_0 as a natural logarithm and use (A2) to obtain the estimate $\frac{N\varrho^N}{(1 - \varrho^N)} > 0$ for this sum.

At the maximum distance of r_2 , the value of Φ^+ vanishes only at the edge of the blue $[\infty]$ region. It follows that ϕ_2^+ must be opposite in sign to ϕ_1^+ at this distance, i.e., it is also positive at maximum distance. This confirms that the internal vortices always rotate in the same direction.

We next analyse the boundary of the yellow $[+/+]$ region shown in Figure 4, where the vortices in the two layers rotate in the same direction. Along this boundary, given by the curve $\tilde{M}(\varrho^+)$, the angular velocity of the external vortices vanishes at the minimum of $r_1 = R$. It thus cannot change sign for any r_1 . The equation for $\tilde{M}(\varrho^+)$ is

$$\begin{aligned} \phi_1^- &= -\frac{\kappa}{4\pi R^2} \left[\sum_{n=1}^{N-1} \gamma R \sin \frac{\pi n}{N} K_1 \left(2\gamma R \sin \frac{\pi n}{N} \right) \right. \\ &+ \left. \gamma R \sum_{n=0}^{N-1} \frac{1 - \varrho \cos \frac{2\pi n}{N}}{G(\varrho, 0, n)} K_1(\gamma R G(\varrho, 0, n)) - \frac{N + 1 + (N - 1)\varrho^N}{2(1 - \varrho^N)} \right]. \end{aligned} \quad (28)$$

This curve coincides with the boundary of the red $[-/+]$ region shown in Figure 4, in the limit $\varrho \ll 1$, and reaches the same limiting point given by Equation (26). There are no

solutions for $\tilde{M} \rightarrow -\infty$ or $\tilde{M} \rightarrow -0$. It follows that the boundaries of the yellow $[+/+]$ and the blue $[\infty]$ regions intersect at a finite value of \tilde{M} (as has been confirmed numerically).

There is a small region between the $[-/+]$ and $[+/+]$ regions, shown in black in Figure 4, where angular velocity of external vortices changes sign over the period T_2 of oscillation. The white curve lying inside this region indicates where the time-averaged angular velocity, $\langle \dot{\phi}_1 \rangle_{T_2}$, vanishes. Along this curve, the external vortices only nutate, with no net rotation over a period.

We next consider the characteristics of the localised, bounded vortex motions. First, we examine angular velocity profiles in a few examples. Figure 13 shows the initial upper-layer and lower-layer profiles $\omega_{1,2}^+ = \dot{\phi}_{1,2}^+$ (the right-hand sides of Equations (7) and (8) at $t = 0$), for $\Phi = \pi/N$ and $N = 3$. In Figure 13a the profiles vary with $\varrho^+ = r_2/r_1$ for two values of $R = r_1$, while in (b) the profiles vary with R for two values of ϱ^+ . In panel (a), the angular velocity profile does not change sign over the entire interval of the parameter ϱ^+ , but the signs are opposite for the upper-layer and lower-layer vortices when $R = 1$ (they move in the direction corresponding to their strength). However, when $R = 4$, both angular velocities are positive, due to the dominant role of the cyclonic lower layer. In Figure 13b in both cases ($\varrho^+ = 0.6$ and $\varrho^+ = 0.8$), ω_1^+ changes sign as R increases, when the upper-layer vortices fall under the prevailing influence the lower-layer vortices.

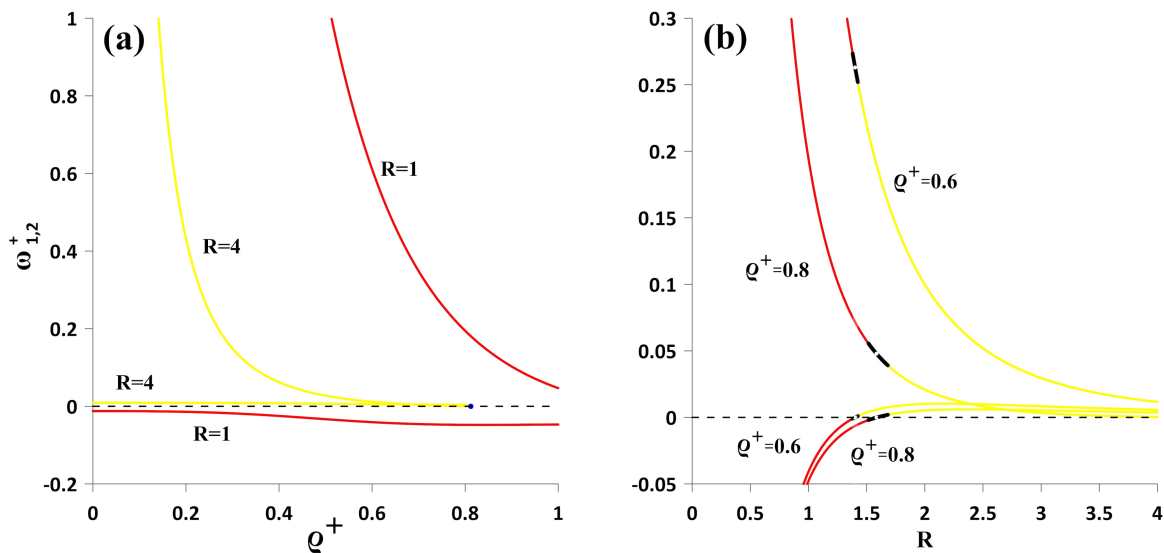


Figure 13. Initial angular velocity profiles of the upper-layer and lower-layer vortices, $\omega_{1,2}^+ = \dot{\phi}_{1,2}^+$, for $N = 3$ and $\Phi = \pi/N$: (a) dependence on ϱ^+ for $R = 1$ and $R = 4$; (b) dependence on R for $\varrho^+ = 0.6$ and $\varrho^+ = 0.8$. The colours of the curves correspond to the colours of the areas in Figure 4b,e, yellow: regions $[+/+]$, and red: region $[-/+]$. The segments of the curves in black correspond to the $[-0 +/+]$ region. The white markers (on the black segments) correspond to the white curve in Figure 4 with zero values of the angular velocity, ω . The blue marker in panel (a) also corresponds to zero angular velocity—this is the stationary state at the boundary of the region of bounded motions. The monotonically decreasing curves in the upper parts of the panels correspond to ω_2^+ ; the other curves (in the lower parts of the panels) correspond to ω_1^+ . A dashed black line is plotted at zero angular velocity.

Following SKDR, we introduce a characteristic of the direction of the upper-layer vortex rotation:

$$\delta_{max} = \frac{T_1}{T_0} = \frac{\langle \omega_2 - \omega_1 \rangle_{T_0}}{\langle \omega_1 \rangle_{T_1}}, \tag{29}$$

where T_0 is the time it takes a vortex to move from its maximum radius to its minimum radius and back, T_1 is the upper-layer vortex rotation period around the origin, and $\langle \dots \rangle_T$ denotes the time average over the interval $[0, T]$. For further insight, the parameter

$\delta = T_1/T_2$, which characterises the ratio of the rotational periods of the vortices in the upper and lower layers, is also useful.

Figure 14 shows examples of the distributions $\delta_{max}(q^+)$, for several values of the angular impulse, \tilde{M} , and for $N = 6$. Here, the red line curve shows $\delta_{max}(q^+)$ when $\tilde{M}/N = -0.1326$, corresponding to the white marker in the upper right corner in Figure 4c, as well as the red vortex trajectories (absolute choreography) in Figure 6, in which $q^+ = 0.9854$. The nonmonotonic character of $\delta_{max}(q^+)$ is consistent with the $[-/+]$ -type of motion, but the monotonically decreasing branch of this distribution corresponds to the $[+/+]$ -type of motion.

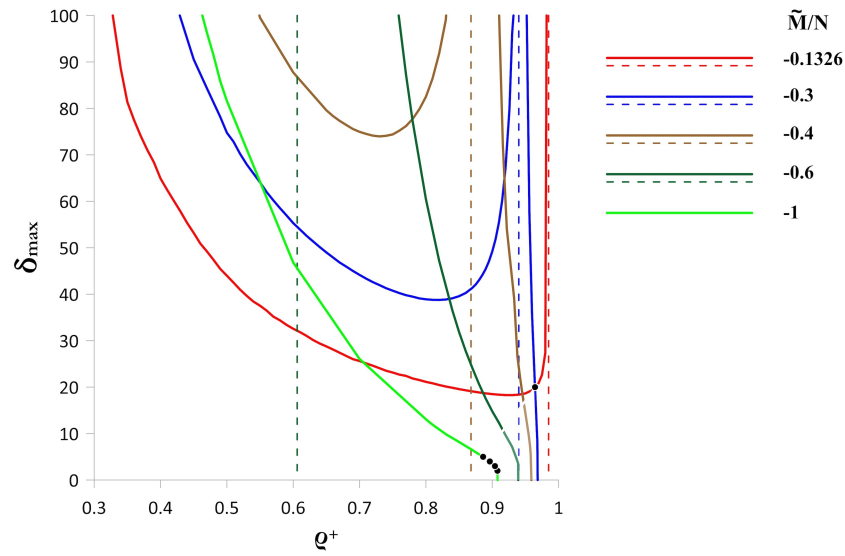


Figure 14. Upper-layer oscillation to rotation period ratio, δ_{max} (limited to the range $[0, 100]$), as a function of q^+ for a hexagonal hetonic array ($N = 6$) for several values of \tilde{M}/N (solid lines). The dashed lines give the asymptotes $\omega^+ = 0$. The markers correspond to pairs of values (δ_{max}, q^+) for the periodic trajectories in Figure 15 ($\delta_{max} = 2, 3, 4$ and 5 on the green line) and Figure 16 ($\delta_{max} = 20$ on the red and blue lines).

According to Figure 4c, when $\tilde{M}/N = -1$ only the $[+/+]$ type of bounded motion occurs (the green line on Figure 14). The two cases $\tilde{M}/N = -0.3$ and -0.4 by contrast contain both bounded and unbounded types of motion. The black markers in Figure 14 indicate the initial conditions for the periodic motions shown in Figures 15 and 16. We see that δ_{max} varies continuously in certain intervals of the parameters q^+ and \tilde{M}/N , with the exception of the resonance values of q^+ when $\omega_1 = 0$. Of particular interest are the cases with integer values of δ_{max} ; they correspond to closed periodic trajectories of the vortex of the upper layer with an integer number of maxima. In view of Remark 1, in this case, the vortex in the lower layer must also move along a closed trajectory, which must also have an integer number of maxima. Thus, the value of δ for such cases is always rational or an integer. Figure 15 shows four examples of stationary periodic trajectories for an equivalent heton. In all cases, the closed shape of the vortex trajectory of the upper layer is such that, as noted above, the number of maxima coincides with value of δ_{max} : at $\delta_{max} = 2$ it resembles an ellipse symmetrically flattened above and below. In the other cases, the trajectories are quasi δ_{max} -gonal in structure. In the lower layer, the situation as a whole is more complicated. For $\delta_{max} = 2$, the trajectory is closed with three maxima of the radial coordinate r_2 and three self-intersection points. For $\delta_{max} = 3$, the trajectory has an oval shape. The number of maximum increases as δ_{max} increases.

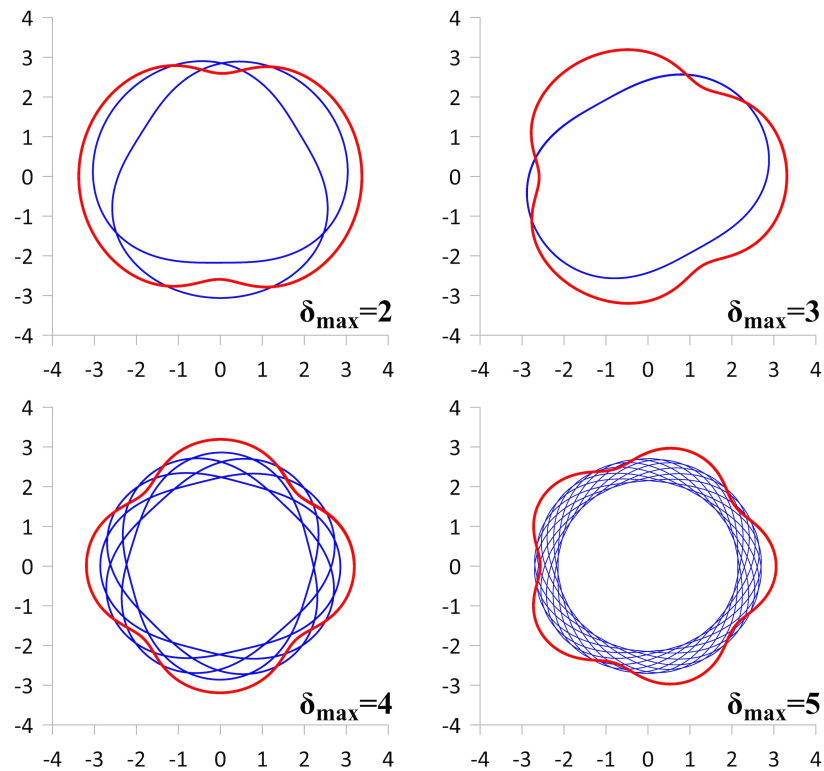


Figure 15. Vortex trajectories of an equivalent heton with $N = 6$ corresponding to stationary periodic solutions, for integer values $\delta_{max} = 2, 3, 4$ and 5 , for $\tilde{M}/N = -1$, and for $q^+ = 0.9078$ ($R = 3.3720, \delta = 4/3$), 0.9041 ($R = 3.3095, \delta = 3/2$), 0.8964 ($R = 3.1906, \delta = 3$) and 0.8863 ($R = 3.0537, \delta = 4$), respectively. These trajectories correspond to the black round markers on the green line in Figure 14.

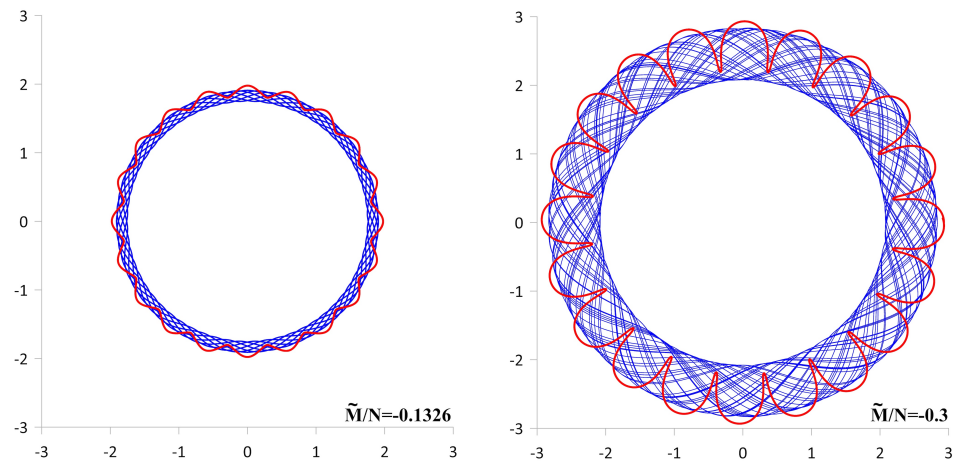


Figure 16. The same as in Figure 15, but for the single value $\delta_{max} = 20$. On the left: $\tilde{M}/N = -0.1326$, $q^+ = 0.96550$ ($R = 1.97761, \delta = 7/4$); on the right: $\tilde{M}/N = -0.3$, $q^+ = 0.96447$ ($R = 2.931942$, $\delta = 17/4$). These trajectories correspond to the black round markers on the red and blue lines in Figure 14.

Figure 16 shows the periodic trajectories for $\delta_{max} = 20$, $\tilde{M}/N = -0.1326$, $q^+ = 0.96550$ (left panel) and $\tilde{M}/N = -0.3$, $q^+ = 0.96447$ (right panel). In the first case, the corresponding marker in Figure 14 lies on the red non-monotonic curve, and in the second it lies on the blue monotonic one. Since the values q^+ are very close for both cases, the markers in Figure 14 are visually indistinguishable. It is important to note that in the first case the solution belongs to the $[-/+]$ type of motion; that is, when the upper-layer vortices rotate,

on average, anticyclonically and the lower-layer vortices rotate cyclonically. In the second case, all vortices rotate cyclonically (region [+ / +]).

Remark 3. Recall that Figures 15 and 16 show the motion of an equivalent heton (i.e., one vortex per layer). The motion of the complete vortex structure is obtained by N -fold symmetry.

Figure 17 shows the trajectories of all the vortices for the cases shown in Figure 15 with $N = 6$. The combined trajectories are 6-fold symmetric, unlike that of the equivalent heton, but are also highly tangled. We discuss the cases with different integer values of δ_{max} in turn.

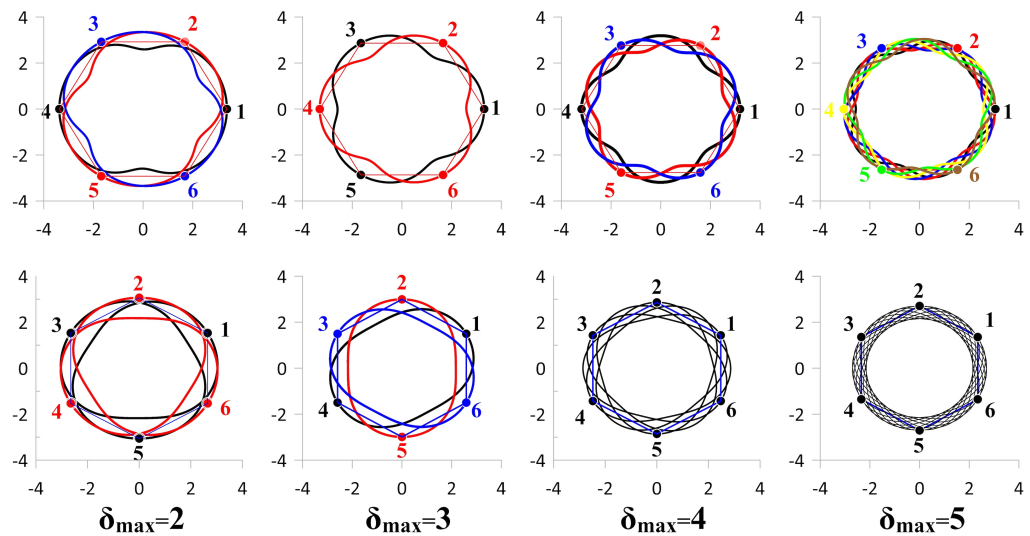


Figure 17. Periodic trajectories of all six vortices ($N = 6$) in each layer (upper/lower row for the upper/lower layer) for $\delta_{max} = 2, 3, 4$ and 5 (left to right). Different colours and line widths are used to distinguish the vortices. The initial positions of the vortices are numbered and coloured the same way as the trajectories emanating from them.

For $\delta_{max} = 2$, there are three distinct trajectories in the upper layer (plotted in black, red and blue) along which vortices (1,4), (2,5) and (4,6) move, respectively. In the lower layer, we observe two distinct trajectories. Vortices 1, 3 and 5 move along the black trajectory, while vortices 2, 4 and 6 move along the red one.

For $\delta_{max} = 3$, now there are only two distinct trajectories in the upper layer, with vortices 1, 3 and 5 moving along the trajectory plotted in black, and vortices 2, 4 and 6 along the trajectory plotted in red. In the lower layer, there are three distinct trajectories along which vortices (1,4), (2,5) and (4,6) move, respectively. This behaviour is exactly the reverse of what was found for $\delta_{max} = 2$. The fact that the vortices move along independent closed curves is characteristic of the vortex motion for low-mode periodic solutions (low integer values of δ_{max}) for $N > 2$.

For $\delta_{max} = 4$, as in the first case, three distinct trajectories are observed in the upper layer, while now all vortices of the lower layer move along a single trajectory. During the full period of revolution around the centre, the radial coordinate of the vortices reaches a maximum twelve times.

The case $\delta_{max} = 5$ stands out from the previous ones, because now, in the upper layer, each of the six vortices moves along its own individual trajectory. This is because $N = 6$ and $\delta_{max} = 5$ are co-prime. Each trajectory is plotted in a different colour in Figure 17. In the lower layer, as before, all the vortices follow one another along one common trajectory, and now the the radial coordinate reaches a maximum thirty times per period.

Thus, in all cases with integer values of δ_{max} , all trajectories are absolute choreographies. In the first two cases, the choreographies are convoluted in both layers, and in

last two cases, the choreographies are convoluted in the upper layer, but simple in the lower layer.

Figure 18 shows three more examples of the trajectories of all six two-layer pairs of vortices for $\tilde{M}/N = -0.1396$. The trajectories of the vortices of the upper layer are plotted in red, while those of the lower layer are plotted in blue. The central part of the figure shows the trajectories of all the vortices for $q^+ = 0.96550$ corresponding to $R = 1.97761$ and $\delta = 7/4$, as previously shown in Figure 16. In this case, vortices (1,6), (2,5) and (3,6) of the upper layer move along three distinct trajectories, while the vortices of the lower layer move along a single trajectory. In the second case, for $q^+ = 0.8954$ corresponding to $R = 3.024729$ and $\delta \rightarrow \infty$, the vortices of the lower layer follow a single trajectory resembling an hexagon with smoothed edges. The vortices of the upper layer move along distinct, closed, peripheral trajectories, as previously shown in Figure 6. In the third case, for $q^+ = 0.8960$ corresponding to $R = 3.088396$ (i.e., a small increase in q^+ from the second case), the vortices scatter as six heton pairs. This is justified by the fact that the second case lies on the boundary between the regions of bounded and unbounded motion shown in the regime diagram in Figure 4.

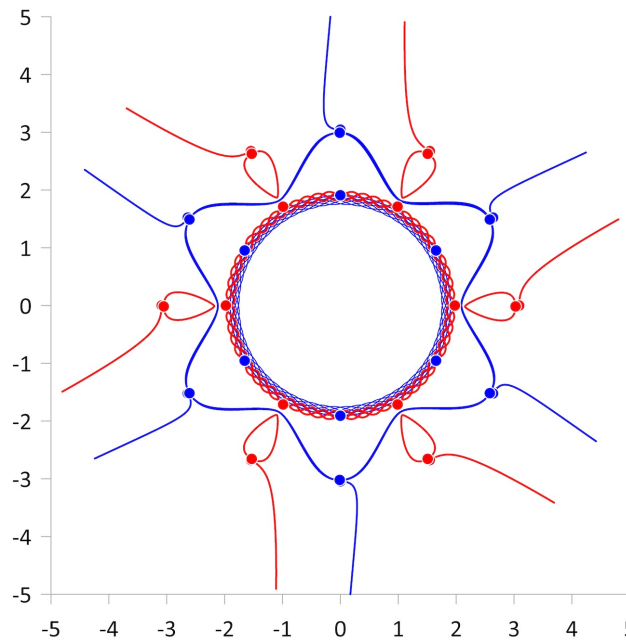


Figure 18. Superimposed vortex trajectories of different $N = 6$ hetons having $\tilde{M}/N = -0.1326$ and (1) $q^+ = 0.9655$, $R = 1.97761$, $\delta = 7/4$, black marker on the red curve in Figure 14 (centre); (2) $q^+ = 0.8954$, $R = 3.024729$, $\delta = \infty$, red asymptote in Figure 14 (intermediate structure) and (3) $q^+ = 0.8960$, $R = 3.088396$ (scattering hetons). Markers indicate the initial positions of the vortices.

4. Finite-Core Hetons

In this section, we present some results for the interaction of finite-core hetons (i.e., hetons comprised vortices with finite area). The hetons have uniform PV, $q = \pm 2\pi$, without loss of generality. Considering finite-core hetons introduces a new length scale to the problem, namely the size of the vortices. Vortices have initially a circular horizontal cross-section of radius R_v . Finite-core vortices have a shape and can deform. The deformation affects the velocity field the vortices induce on each other. Vortices can also strongly interact and merge when close together. No symmetry is imposed in the nonlinear evolution, and perturbations (including asymmetric ones) are allowed to develop. Simulations are run using Contour Surgery with the method’s standard set-up [70]. Equations are marched in time using a fourth-order Runge–Kutta scheme with a time step set by the vortices PV: $\Delta t = \pi/(10q)$.

In the first set of numerical experiments, we revisit the point-vortex case for $N = 3$, $\tilde{M}/N = -0.28$ and $q^+ = 0.8892$ shown in Figure 5c, but now for finite-core vortices. We first consider vortices of small to moderate radius, specifically $R_v = 0.1, 0.2, 0.3, 0.4$ and 0.5 . We keep $\tilde{M}/N = -0.28$ fixed and we determine the value of $q^+(R_v)$ corresponding to quasi-closed trajectories (absolute choreographies) for the vortex centres, by trial and error. The values of $q^+(R_v)$ thereby obtained are listed in Table 1.

Table 1. Values of q^+ for an absolute choreography for $N = 3$ and $\tilde{M}/N = -0.28$ for various initial radii R_v .

R_v	0.05	0.1	0.2	0.3	0.4	0.5
q^+	0.8897	0.8904	0.8935	0.8978	0.9025	0.9078

The values of $q^+(R_v)$ are remarkably close to the value obtained for point vortex hetons, and the maximum relative departure for the largest hetons considered, $R_v = 0.5$, is only about 2%.

Figure 19 shows both the long-time trajectories of the centre of the first vortex in each layer (in black), as well as the shape of the bounding contour for all six vortices at various times (in blue for the anticyclones in the upper layer, and in red for the cyclones in the lower layer).

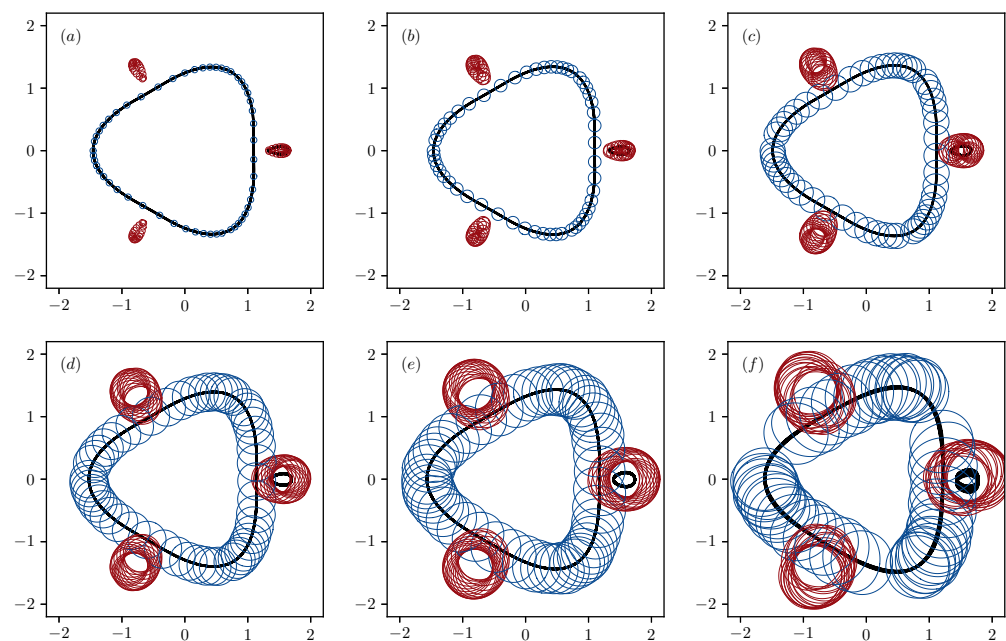


Figure 19. Trajectories for the first vortices in each layer (black lines) $N = 3$, $\tilde{M}/N = -0.28$, (a): $R_v = 0.05$, $q^+ = 0.8897$, (b): $R_v = 0.1$, $q^+ = 0.8904$, (c): $R_v = 0.2$, $q^+ = 0.8935$, (d): $R_v = 0.3$, $q^+ = 0.8978$, (e): $R_v = 0.4$, $q^+ = 0.9025$, (f): $R_v = 0.5$, $q^+ = 0.9078$. The blue (respectively, red) contours show the vortex boundaries in the upper (respectively, lower) layer at various times.

We next measure the vortex deformation by evaluating the semi-axis lengths a and b , with $a > b$ without loss of generality. We perform this by fitting ellipses having the same second-order spatial moments to the actual vortex bounding contours (see, e.g., [63]). As R_v is increased while keeping the other parameters fixed, as expected, the vortex deformation becomes more significant, as shown in Figure 20 for the first vortex of the upper layer. Instead of moving along a unique trajectory, the vortices move along criss-crossing trajectories without deviating far from a mean line overall. This is a consequence of the deformation of the vortices shown in Figure 20. The apparent thickness of the black

lines (increasing with R_v) showing the vortex trajectories, in fact, indicates the spread of the trajectories.

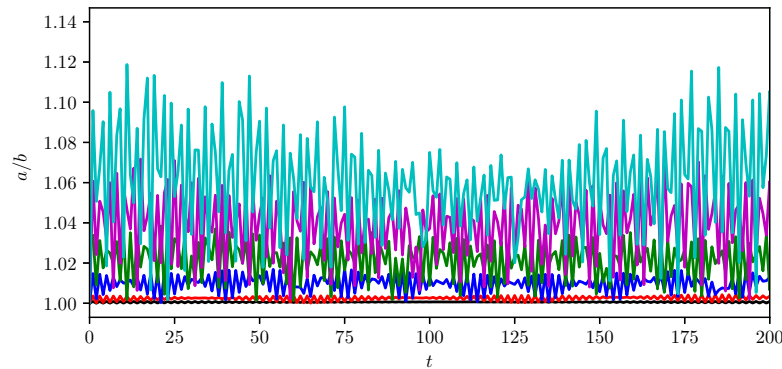


Figure 20. Evolution of the aspect ratio a/b of vortex 1 in layer 1 for $N = 3$, $\tilde{M}/N = -0.28$, and $R_v = 0.05$, $\varrho^+ = 0.8897$ (black), $R_v = 0.1$, $\varrho^+ = 0.8904$ (red) $R_v = 0.2$, $\varrho^+ = 0.8978$ (blue), $R_v = 0.3$, $\varrho^+ = 0.8978$ (green), $R_v = 0.4$, $\varrho^+ = 0.9025$ (magenta) $R_v = 0.5$, $\varrho^+ = 0.9078$ (cyan).

When R_v is increased further, the relative distance ℓ/R_v , where ℓ is a typical scale of the distance between the vortex centres in a given layer, decreases, and vortices are likely to strongly interact. Figure 21 shows such a strong interaction for $N = 3$, $\tilde{M}/N = -0.28$ and $\varrho = 0.9073$, i.e., close to the corresponding absolute choreography for larger vortices $R_v = 0.8$. The three cyclonic vortices of the lower layer deform strongly, and merge first in the centre of the domain. Three secondary satellite vortices form and are ejected away from the centre. This is a consequence of the invariance of the angular impulse M , and the migration of positive PV towards the centre of the lower layer.

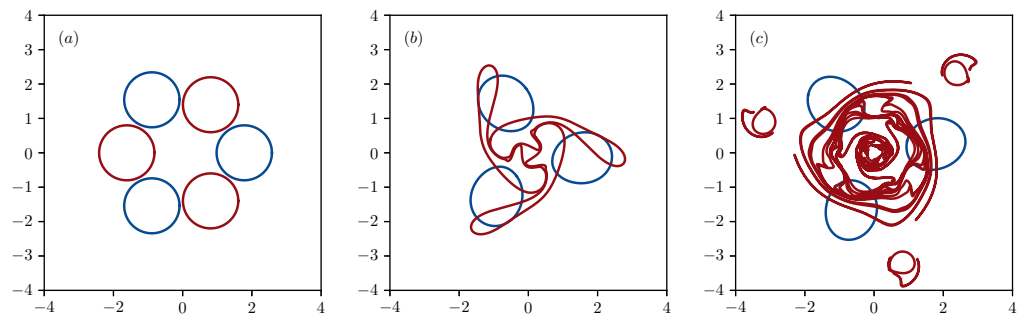


Figure 21. Top view on the vortex bounding contours for $N = 3$, $\tilde{M} = -0.28$, $R_v = 0.8$, $\varrho^+ = 0.9073$ at $t = 0$ (a), $t = 5$ (b), and $t = 12$ (c).

We next consider the interaction between six hetons close to the regime of absolute choreography for $\tilde{M}/N = -0.3$. For $R_v = 0.2$, we recover the absolute choreography for $\varrho^+ = 0.965$ (see Figure 22a). With increasing R_v , obtaining absolute choreographies for long times becomes difficult: numerical results indicate that the configuration is or becomes unstable. For $R_v = 0.5$ and $\varrho^+ = 0.9678$, when $t \leq 280$, the vortices move along quasi-closed trajectories, as seen in Figure 22b. They however depart from them at later times, as shown in Figure 22c.

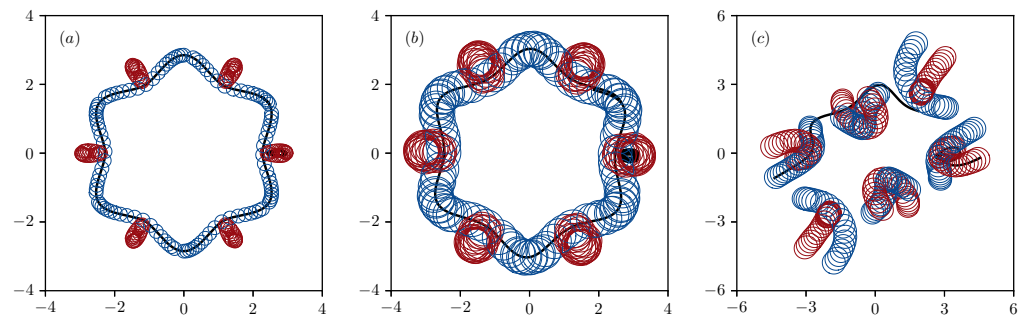


Figure 22. Trajectories: $N = 3$, $\tilde{M}/N = -0.3$, (a): $R_v = 0.2$, $q^+ = 0.965$, (b): $R_v = 0.5$, $q^+ = 0.9678$ for $0 \leq t \leq 280$. (c): same as (b) but for $280 < t < 408$.

5. Discussion and Concluding Remarks

In SKDR, we analysed the motion of an N -symmetric two-layer system of $2N$ vortices for the special case $N = 2$. In the present paper, we have extended these results to the case of arbitrary N . Diagrams of all possible regimes of motion have been established and analysed. Numerous examples of vortex trajectories have been considered, mainly for $N = 3$ and $N = 6$. Particular attention has been paid to the study of the properties of relative and absolute choreographies, both simple and complex [64]. Note that all the results of the calculations and the analysis presented in this article for $r_1 < r_2$ are new, and have not previously been considered by other authors. We can only note the work [2], where test calculations were carried out for the cases $N = 2$ and $N = 6$, but at $r_1 = r_2$.

The concept of a two-layer quasi-geostrophic heton is attractive, first of all, because it is the simplest model for the horizontal transfer of temperature anomalies. The vortex structures considered in this work, with anticyclones in the upper layer and cyclones in the lower layer, depress the interface between the layers. Thus, any vortex motion is accompanied by the transport of a fluid column warmer than the surrounding medium. So, the following ‘thermal’ interpretation can be given to the numerical experiments shown in Figure 18.

1. $q^+ = 0.9655$: A regular mixing of warm water in both layers occurs inside an annular region, somewhat wider than the area occupied by the trajectories. The total transfer of warm fluid occurs in the cyclonic direction (type [+/+]).
2. $q^+ = 0.8954$: All the vortices of the lower layer move along a single trajectory in the cyclonic direction, and all the vortices of the upper layer move in the anticyclonic direction along another peripheral closed curves (type [0/+]). Both sets of vortices carry with them columns of fluid that are warmer than their surroundings.
3. $q^+ = 0.8960$: the twelve vortices form six two-layer pairs with tilted axes, which scatter radially while preserving the N -fold symmetry of the system, and carrying warm water (motion type [∞]).

In the general case, bounded motions of N -symmetric warm hetons are accompanied either by cyclonic transport of warm water column from surface to bottom, or cyclonic transport in the lower layer and anticyclonic in the upper layer inside an annular area. Unbounded motions expel the warmer fluid radially, away from its initial location. A similar transport of cold water would occur if the hetons were cold instead.

Finally, we have shown a few selected examples that the idealised point vortex trajectories are reproduced for more realistic finite core hetons, so long as the vortices are not too large. Large vortices may strongly interact in the nonlinear regime.

In this paper, we have not addressed the stability of stationary configurations. This will be addressed in a future paper. We expect that the motions of unstable configurations may also be irregular, breaking the initial symmetry of the heton.

Author Contributions: Conceptualization K.V.K. and M.A.S.; Methodology K.V.K., M.A.S., D.G.D. and J.N.R.; Writing—original draft preparation K.V.K. and M.A.S.; Writing—review and editing, D.G.D. and J.N.R. All authors have read and agreed to the published version of the manuscript.

Funding: This research received no external funding

Institutional Review Board Statement: Not applicable.

Informed Consent Statement: Not applicable.

Data Availability Statement: The data presented in this study are available on request from the corresponding author. The data are not publicly available as they are easy to reproduce.

Conflicts of Interest: The authors declare no conflicts of interest.

Appendix A. Some Useful Formulas and Results

One can write

$$\begin{aligned} \sum_{n=0}^{N-1} \sin\left(\frac{\pi l}{N} + \frac{2\pi n}{N}\right) F\left[f\left(\frac{l\pi}{N} + \frac{2\pi n}{N}\right)\right] &= \sum_{n=1}^N \sin\left(\frac{\pi l}{N} + \frac{2\pi n}{N}\right) F\left[f\left(\frac{l\pi}{N} + \frac{2\pi n}{N}\right)\right] = \\ &= \sum_{n=-l+1}^{N-l} \sin\left(\frac{\pi l}{N} + \frac{2\pi(l+n)}{N}\right) F\left[f\left(\frac{l\pi}{N} + \frac{2\pi(l+n)}{N}\right)\right] = \\ \sum_{n=0}^{N-1} \sin\left(\frac{\pi l}{N} + \frac{2\pi(l+(N-l)-n-l)}{N}\right) F\left[f\left(\frac{l\pi}{N} + \frac{2\pi(l+(N-l)-n-l)}{N}\right)\right] &= \\ &= - \sum_{n=0}^{N-1} \sin\left(\frac{\pi l}{N} + \frac{2\pi n}{N}\right) F\left[f\left(-\frac{l\pi}{N} - \frac{2\pi n}{N}\right)\right]. \end{aligned} \tag{A1}$$

It follows that the sum is equal to zero. Here, $l \geq 1$, is an arbitrary continuous function (K_0 or K_1 for our purposes), and f is an odd periodic function, for example $\cos\left(\frac{l\pi}{N} + \frac{2\pi n}{N}\right)$.

We have used the following products

$$\begin{aligned} \prod_{n=0}^{N-1} \left(q^2 - 2q \cos\left(x + \frac{2\pi n}{N}\right) + 1 \right) &= q^{2N} - 2q^N \cos Nx + 1, \\ \prod_{n=1}^{N-1} \sin \frac{\pi n}{N} &= 2^{1-N} N, \end{aligned} \tag{A2}$$

to obtain the Hamiltonian (11).

Let us recall the formula

$$\begin{aligned} \cos^{2J} A &= \frac{1}{2^{2J}} \left[\binom{2J}{J} + 2 \sum_{j=0}^{J-1} \binom{2J}{j} \cos(2J-2j)A \right] \\ &= \frac{1}{2^{2J}} \left[\frac{(2J)!}{(J!)^2} + \dots + 2 \cos 2JA \right], \\ \cos^{2J+1} A &= \frac{2}{2^{2J+1}} \sum_{j=0}^J \binom{2J+1}{j} \cos(2J+1-2j)A \\ &= \frac{2}{2^{2J+1}} (\cos(2J+1)A + \dots). \end{aligned} \tag{A3}$$

From (A3), it follows that

$$\sum_{n=0}^{N-1} \left[\frac{j+1}{j} \cos^{j+1}\left(\Phi + \frac{2\pi n}{N}\right) - \cos^{j-1}\left(\Phi + \frac{2\pi n}{N}\right) \right] = 0, \tag{A4}$$

if $j < N - 1$, and

$$\sum_{n=0}^{N-1} \left[\frac{N}{N-1} \cos^N \left(\Phi + \frac{2\pi n}{N} \right) - \cos^{N-2} \left(\Phi + \frac{2\pi n}{N} \right) \right] = \frac{N^2 \cos N\Phi}{(N-1)2^{N-1}} \quad (A5)$$

if $j = N - 1$.

The following relationship is also useful to estimate the sign of the vortex rotation:

$$\gamma R \varrho \sum_{n=0}^{N-1} \frac{\varrho - \cos \left(\Phi + \frac{2\pi n}{N} \right)}{G(\varrho, \Phi, n)} K_1(\gamma R G(\varrho, \Phi, n)) = -\varrho \frac{\partial}{\partial x} \sum_{n=0}^{N-1} K_0(\gamma R G(x, \Phi, n)) \Big|_{x=\varrho}. \quad (A6)$$

Appendix B. Extreme Properties of the Hamiltonian

Let us consider the derivatives of the Hamiltonian at the extrema. In the case $\gamma R G(\varrho, \Phi, n) \geq 1$, the sums in (12) are exponentially small. One can write

$$\begin{aligned} \frac{4\pi}{\kappa^2} \frac{\partial H}{\partial \varrho} &\sim \frac{\partial}{\partial \varrho} \left[\ln R^2 \left(1 + \varrho^N \left(\varrho^N - 2 \cos N\Phi \right) \right) - \ln \varrho^{N-1} \right] = \\ &= -\frac{1}{\varrho(1-\varrho^2)} \left[\frac{N(1-\varrho^{2N})(1-\varrho^2)}{1+\varrho^N(\varrho^N-2\cos N\Phi)} - (1+\varrho^2) \right]. \end{aligned} \quad (A7)$$

We can see that, for small enough ϱ , the derivative is negative for any value of Φ . For larger ϱ , we use the equation

$$\varrho = 1 - \frac{\delta}{N}, \quad \delta \ll N. \quad (A8)$$

Now, we can write

$$\frac{4\pi}{\kappa^2} \frac{\partial H}{\partial \varrho} \sim -\frac{2}{\varrho(1-\varrho^2)} \left[\frac{(1-e^{-2\delta})\delta}{1+e^{-\delta}(e^{-\delta}-2\cos N\Phi)} - \left(1 + \frac{\delta}{N} \right) \right]. \quad (A9)$$

For the case $\Phi = 0$, we have

$$\frac{4\pi}{\kappa^2} \frac{\partial H^-}{\partial \varrho} \sim -\frac{2}{\varrho(1-\varrho^2)} \left[\frac{(1+e^{-\delta})\delta}{1-e^{-\delta}} - 1 + O\left(\frac{1}{N}\right) \right]. \quad (A10)$$

One can see that the derivative of $H^- = H(\Phi = 0, \varrho)$ is always negative.

For the case $\Phi = \pi/N$, we have

$$\frac{4\pi}{\kappa^2} \frac{\partial H^+}{\partial \varrho} \sim -\frac{2}{\varrho(1-\varrho^2)} \left[\frac{(1-e^{-\delta})\delta}{1+e^{-\delta}} - 1 + O\left(\frac{1}{N}\right) \right]. \quad (A11)$$

Here, the situation is different. The derivative of $H^+ = H(\Phi = \pi/N, \varrho)$ changes sign. It means that the function $H^+(\varrho)$ has a minimum at some value $\varrho = \varrho^*$. For the case above, the critical value of ϱ is $\varrho^* \approx 1 - \frac{1.545}{N}$.

We should consider now the case $\gamma R G(\varrho, \Phi, n) \leq 1$. Let us expand the Bessel functions:

$$\begin{aligned} \frac{4\pi}{\kappa^2} \frac{\partial H}{\partial \varrho} &= \frac{\partial}{\partial \varrho} \left[\ln \frac{1 + \varrho^N (\varrho^N - 2 \cos N\Phi)}{R^{4(N-1)} \varrho^{2(N-1)}} - \sum_{n=0}^{N-1} \ln G^2(\varrho, \Phi, n) + O(R) \right] \\ &= \frac{\partial}{\partial \varrho} \left[-4(N-1) \ln R - 2(N-1) \ln \varrho + O(R) \right] \\ &= -2(N-1) \frac{1 + \varrho^2}{\varrho(1-\varrho^2)} + O(R^2). \end{aligned} \quad (A12)$$

One can see that, in this case, the derivative of Hamiltonian is always negative for any value of Φ .

However, the constraint $\gamma RG(\varrho, \Phi, n) \leq 1$ depends on the value of ϱ . We now consider a small $-\tilde{M}$. Then,

$$\gamma RG\left(\varrho, \frac{\pi}{N}, n\right) = \gamma \sqrt{\frac{2}{N} \frac{\tilde{M}}{1-\varrho^2} \left[1 + \varrho \left(\varrho - 2 \cos \frac{\pi(1+2n)}{N}\right)\right]}. \tag{A13}$$

Even if $-\tilde{M}$ is small, $\gamma RG(\varrho, \Phi, n)$ can grow as $\varrho \rightarrow 1$. We again use $\varrho = 1 - \frac{\delta}{N}$, and obtain

$$\begin{aligned} \gamma RG\left(\varrho, \frac{\pi}{N}, n\right) &= \gamma \sqrt{\frac{2\tilde{M}}{N} \left(\frac{1-\varrho}{1+\varrho} + \frac{4\varrho \sin^2 \frac{\pi(1+2n)}{N}}{1-\varrho^2}\right)} \\ &\sim \gamma \sqrt{\frac{\tilde{M}}{N} \left(\frac{\delta}{N} + \frac{4N \sin^2 \frac{\pi(1+2n)}{N}}{\delta}\right)}. \end{aligned} \tag{A14}$$

We also have $R > 1$, if δ is small enough, i.e., such that $\gamma RG(\varrho, \Phi, n) \geq 1$. Thus, the derivative of the Hamiltonian is negative again for the case $\Phi = 0$, due to (A10). And, the derivative of Hamiltonian changes sign for the case $\Phi = \pi/N$, but for a larger value of ϱ^* than for the case of a large $-\tilde{M}$. We can roughly estimate ϱ^* for small $-\tilde{M}$. For this we estimate the derivative of H as

$$\begin{aligned} \frac{4\pi(1-\varrho^2)\varrho}{2\kappa^2} \frac{\partial H^+}{\partial \varrho} &= 1 - 2 \sum_{j=1}^J \frac{\gamma R \pi}{N} j K_1\left(\frac{\gamma R \pi}{N} j\right) + \frac{\gamma R \pi}{N} K_1\left(\frac{\gamma R \pi}{N}\right) \\ &+ O(\delta) + O\left(\left(N - \frac{J}{2}\right) \sqrt{\gamma R \left(\frac{2\pi J}{N}\right)} \exp\left(-\sqrt{\gamma R \left(\frac{2\pi J}{N}\right)}\right)\right) = 0 \end{aligned} \tag{A15}$$

Here, we have taken into account Equation (A14) and the exponential decrease in the Modified Bessel function as j grows. For finite $J \ll N$, we can solve Equation (A15) for $\frac{\gamma R \pi}{N}$. We find that

$$\begin{aligned} \frac{\gamma R \pi}{N} &\approx 1.13; \quad -\tilde{M} \approx 0.638 \frac{N^3}{\gamma^2 \pi^2} (1-\varrho^2), \quad (J = 2); \\ \frac{\gamma R \pi}{N} &\approx 1.286; \quad -\tilde{M} \approx 0.827 \frac{N^3}{\gamma^2 \pi^2} (1-\varrho^2), \quad (J = 14). \end{aligned} \tag{A16}$$

The solution changes very little for a larger J .

We also need to analyse the second derivative with respect to Φ :

$$\frac{4\pi}{\kappa^2} \frac{\partial^2 H}{\partial \Phi^2} = \frac{\partial^2}{\partial \Phi^2} \left[\ln\left(1 + \varrho^N (e^N - 2 \cos N\Phi)\right) + \sum_{n=0}^{N-1} K_0(\gamma RG(\varrho, \Phi, n)) \right]. \tag{A17}$$

We again begin with the case $\gamma RG(\varrho, \Phi, n) \geq 1$, when the Modified Bessel functions are exponentially small,

$$\frac{4\pi}{\kappa^2} \frac{\partial^2 H}{\partial \Phi^2} = \frac{\partial^2}{\partial \Phi^2} \ln\left(1 + \varrho^N (e^N - 2 \cos N\Phi)\right) = 2\varrho^N N^2 \left[\frac{\cos N\Phi (1 + \varrho^{2N}) - 2\varrho^N}{(1 + \varrho^N (e^N - 2 \cos N\Phi))^2} \right]. \tag{A18}$$

One can see that we have

$$\frac{4\pi}{\kappa^2} \frac{\partial^2 H^-}{\partial \Phi^2} = \frac{2\varrho^N N^2}{(1-\varrho^N)^2} > 0, \quad \frac{4\pi}{\kappa^2} \frac{\partial^2 H^+}{\partial \Phi^2} = \frac{-2\varrho^N N^2}{(1+\varrho^N)^2} < 0. \tag{A19}$$

Next, we analyse the case $\gamma RG(\varrho, \Phi, n) \leq 1$. Let us expand the Bessel function in (A17):

$$\begin{aligned} \frac{4\pi}{\kappa^2} \frac{\partial^2 H}{\partial \Phi^2} &= \frac{\partial^2}{\partial \Phi^2} \left[\ln \left(1 + \varrho^N \left(\varrho^N - 2 \cos N\Phi \right) \right) + 2 \sum_{n=0}^{N-1} K_0(\gamma RG(\varrho, \Phi, n)) \right] = \\ &- \frac{(\gamma R)^2 \varrho}{4} \sum_{n=0}^{N-1} \left[\cos \left(\Phi + \frac{2\pi n}{N} \right) \ln G^2(\varrho, \Phi, n) + \frac{2\varrho \sin^2 \left(\Phi + \frac{2\pi n}{N} \right)}{G^2(\varrho, \Phi, n)} + O(\gamma R) \right]. \end{aligned} \tag{A20}$$

Here, we take into account that the sums from $\cos(\Phi + \frac{2\pi n}{N})$ and $\sin(\Phi + \frac{2\pi n}{N})$ are equal to zero. We expand this expression as a power series in $\frac{2\varrho}{1+\varrho^2} < 1$:

$$\begin{aligned} \frac{4\pi}{\kappa^2} \frac{\partial^2 H}{\partial \Phi^2} &= \frac{(\gamma R)^2 \varrho}{4} \sum_{m=1}^{\infty} \left(\frac{2\varrho}{1+\varrho^2} \right)^m \sum_{n=0}^{N-1} \left[\frac{m+1}{m} \cos^{m+1} \left(\Phi + \frac{2\pi n}{N} \right) - \cos^{m-1} \left(\Phi + \frac{2\pi n}{N} \right) \right] \\ &+ O((\gamma R)^3). \end{aligned} \tag{A21}$$

Then, using (A5), we obtain the estimate

$$\frac{4\pi}{\kappa^2} \frac{\partial^2 H}{\partial \Phi^2} = \frac{(\gamma R)^2 \varrho}{4} \left(\frac{\varrho}{1+\varrho^2} \right)^{N-1} \frac{N^2}{N-1} \cos N\Phi + O\left(\left(\frac{\varrho}{1+\varrho^2} \right)^N \right) + O((\gamma R)^3). \tag{A22}$$

Thus, in the case $\gamma RG(\varrho, \Phi, n) \leq 1$, we again have a positive second derivative at $\Phi = 0$ and negative one at $\Phi = \pi N$.

Consider the Hamiltonian limiting values. When $\varrho \rightarrow 0$, the Hamiltonian tends to infinity, irrespective of the value of Φ :

$$\begin{aligned} \frac{4\pi H}{\kappa^2} &\sim - (N-1) \ln \varrho + \ln R^2 + \varrho^N \left(\varrho^N - 2 \cos N\Phi \right) + 2 \sum_{n=0}^{N-1} K_0(\gamma RG(\varrho, \Phi, n)) \\ &+ \sum_{n=1}^{N-1} \left[K_0 \left(2\gamma R \sin \frac{\pi n}{N} \right) + K_0 \left(2\gamma R \varrho \sin \frac{\pi n}{N} \right) \right]. \end{aligned} \tag{A23}$$

Here, the sums are always positive, and one can chose a ϱ small enough such that $-(N-1) \ln(\varrho)$ will be larger than any other term in first line, even if R is very small. This means that both H^+ and H^- are positive, and tend to infinity when ϱ tends to zero.

For the case $\Phi = \pi/N$, we have

$$\frac{4\pi H^+}{\kappa^2} \sim \ln 2NR^2 \left(1 - (\varrho^+)^2 \right) - \ln \delta + \sum_{n=1}^{N-1} (\dots) \tag{A24}$$

and the sums in (12) are again positive. This means that H^+ is positive and tends to infinity when $\varrho \rightarrow 1$.

For the case $\Phi = 0$, it was shown above that $RG(\varrho^-, 0, n), R \rightarrow \infty$ for $n \neq 0, N$ and $\varrho \rightarrow 1$. We obtain the estimate

$$\begin{aligned} \frac{4\pi H^-}{\kappa^2} &\sim \ln \frac{R^2 \left(1 - (\varrho^-)^2 \right) \left(1 - (\varrho^-)^N \right)^2}{\left(1 - (\varrho^-)^2 \right) (\varrho^-)^{N-1}} + 2K_0 \left(\gamma \sqrt{R^2 \left(1 - (\varrho^-)^2 \right) \frac{1 - \varrho^-}{1 + \varrho^-}} \right) \\ &\sim \ln \frac{R^2 \left(1 - (\varrho^-)^2 \right) \delta N}{2} - 2 \left(\ln \gamma \sqrt{R^2 \left(1 - (\varrho^-)^2 \right) \frac{1 - \varrho^-}{1 + \varrho^-}} + \gamma_e \right) \\ &= 2 \left(\ln \frac{N}{\gamma} - \gamma_e \right), \end{aligned} \tag{A25}$$

where $\gamma_e \approx 0.5772$ is Euler’s constant. This means that H^- tends to finite constant as $\varrho \rightarrow 1$. Next, let us analyse the difference

$$\frac{4\pi(H^+ - H^-)}{\kappa^2} = 2 \ln\left(\frac{1 + \varrho^N}{1 - \varrho^N}\right) + 2 \sum_{n=0}^{N-1} \left[K_0\left(\gamma R G\left(\varrho, \frac{\pi}{N}, n\right)\right) - K_0\left(\gamma R G\left(\varrho, 0, n\right)\right) \right]. \tag{A26}$$

If the arguments of K_0 are sufficiently large, the sums are exponentially small, and difference is positive and very small for $\varrho < \varrho^*$. For small R , we can use the power series for K_0 [71]

$$2 \sum_{n=0}^{N-1} \left[K_0\left(\gamma R G\left(\varrho, \frac{\pi}{N}, n\right)\right) - K_0\left(\gamma R G\left(\varrho, 0, n\right)\right) \right] \sim - \sum_{n=0}^{N-1} \ln \frac{G^2\left(\varrho, \frac{\pi}{N}, n\right)}{G^2\left(\varrho, 0, n\right)} - \frac{(\gamma R)^2}{8} \sum_{n=0}^{N-1} \left(G^2\left(\varrho, \frac{\pi}{N}, n\right) \ln G^2\left(\varrho, \frac{\pi}{N}, n\right) - G^2\left(\varrho, 0, n\right) \ln G^2\left(\varrho, 0, n\right) \right) \tag{A27}$$

We can represent the expression under the sum as an integral, and expand it in a power series:

$$\begin{aligned} & - \frac{(\gamma R)^2}{8} \sum_{n=0}^{N-1} \left[G^2\left(\varrho, \frac{\pi}{N}, n\right) \ln G^2\left(\varrho, \frac{\pi}{N}, n\right) - G^2\left(\varrho, 0, n\right) \ln G^2\left(\varrho, 0, n\right) \right] \\ &= - \frac{(\gamma R)^2 2\varrho}{8} \int_0^{\frac{\pi}{N}} \sum_{n=0}^{N-1} \sin\left(\Phi + \frac{2\pi n}{N}\right) \ln\left(1 - \frac{2\varrho}{1 + \varrho^2} \cos\left(\Phi + \frac{2\pi n}{N}\right)\right) d\Phi \\ &\sim \frac{1}{2} \frac{(\gamma R)^2 N\varrho}{N-1} \left(\frac{\varrho}{1 + \varrho^2}\right)^{N-1} + o\left((\gamma R)^2\right) + o\left(\varrho \left(\frac{\varrho}{1 + \varrho^2}\right)^{N-1}\right) > 0. \end{aligned} \tag{A28}$$

Finally, we have

$$\frac{4\pi(H^+ - H^-)}{\kappa^2} = \frac{1}{2} \frac{(\gamma R)^2 N\varrho}{N-1} \left(\frac{\varrho}{1 + \varrho^2}\right)^{N-1} + o\left((\gamma R)^2\right) + o\left(\varrho \left(\frac{\varrho}{1 + \varrho^2}\right)^{N-1}\right) > 0. \tag{A29}$$

We can also estimate the amplitude of oscillation $\varrho^+ - \varrho^- \approx -\frac{H^+(\varrho^-) - H^-(\varrho^-)}{\frac{\partial H^+(\varrho^-)}{\partial \varrho}}$. For a sufficiently large R and a small ϱ , we have

$$\varrho^+ - \varrho^- \sim \frac{4(\varrho^-)^{N+1}}{N-1}. \tag{A30}$$

When both R and ϱ are small, we have

$$\varrho^+ - \varrho^- \sim \frac{1}{4} \frac{(\gamma R)^2 N\varrho}{(N-1)^2} \left(\frac{\varrho}{1 + \varrho^2}\right)^N. \tag{A31}$$

References

1. Hogg, N.G.; Stommel, H.M. The heton, an elementary interaction between discrete baroclinic geostrophic vortices, and its implications concerning eddy heat-flow. *Proc. R. Soc. Lond. Math. Phys. Sci.* **1985**, *397*, 1–20.
2. Hogg, N.G.; Stommel, H.M. Hetonic explosions: the breakup and spread of warm pools as explained by baroclinic point vortices. *J. Atmos. Sci.* **1985**, *42*, 1465–1476. [CrossRef]
3. Gryanik, V.M. Dynamics of singular geostrophic vortices in a two-level model of atmosphere (ocean). *Izvestiya Atmos. Ocean. Phys.* **1983**, *19*, 171–179.
4. Chao, S.-Y.; Shaw, P.-T. Eddy maintenance and attrition in a vertically sheared current under Arctic ice. *J. Phys. Oceanogr.* **1998**, *28*, 2427–2443. [CrossRef]
5. Chao, S.-Y.; Shaw, P.-T. Close interactions between two pairs of heton-like vortices under sea ice. *J. Geophys. Res.* **1999**, *104*, 23591–23605. [CrossRef]

6. Chao, S.-Y.; Shaw, P.-T. Fission of heton-like vortices under sea ice. *J. Oceanogr.* **1999**, *55*, 65–78. [[CrossRef](#)]
7. Chao, S.-Y.; Shaw, P.-T. Slope-enhanced fission of salty hetons under sea ice. *J. Phys. Oceanogr.* **2000**, *30*, 2866–2882. [[CrossRef](#)]
8. Chao, S.-Y.; Shaw, P.-T. Heton shedding from submarine-canyon plumes in an Arctic boundary current system: Sensitivity to the undercurrent. *J. Phys. Oceanogr.* **2003**, *33*, 2032–2044. [[CrossRef](#)]
9. Fernando, H.J.S.; Chen, R.; Ayotte, B.A. Development of a point plume in the presence of background rotation. *Phys. Fluids* **1998**, *10*, 2369–2383. [[CrossRef](#)]
10. Fernando, H.J.S.; Smith IV D.C. Vortex structure in geophysical convection. *Eur. J. Mech. B/Fluids* **2001**, *20*, 437–470. [[CrossRef](#)]
11. Gryanik, V.M.; Sokolovskiy, M.A.; Verron, J. Dynamics of heton-like vortices. *Regul. Chaotic Dyn.* **2006**, *11*, 417–438. [[CrossRef](#)]
12. Klinger, B.A.; Marshall, J. Regimes and scaling laws for rotating deep convection in the ocean. *Dyn. Atmos. Oceans* **1995**, *21*, 221–256. [[CrossRef](#)]
13. Legg, S.; Jones, H.; Visbeck, M. A heton perspective of baroclinic eddy transfer in localized open ocean convection. *J. Phys. Oceanogr.* **1996**, *26*, 2251–2266. [[CrossRef](#)]
14. Legg, S.; Marshall, J. A heton model of the spreading phase of open-ocean deep convection. *J. Phys. Oceanogr.* **1993**, *23*, 1040–1056. [[CrossRef](#)]
15. Legg, S.; Marshall, J. The influence of the ambient flow on the spreading of convected water masses. *J. Marine Res.* **1998**, *56*, 107–139. [[CrossRef](#)]
16. Legg, S.; McWilliams, J.; Gao, J. Localization of deep ocean convection by a mesoscale eddy. *J. Phys. Oceanogr.* **1998**, *28*, 944–970. [[CrossRef](#)]
17. Morel, Y.; McWilliams, J. Effect of isopycnal and diapycnal mixing on the stability of oceanic currents. *J. Phys. Oceanogr.* **2001**, *31*, 2280–2296. [[CrossRef](#)]
18. Oliver, K.I.C.; Eldevik, T.; Stevens, D.P.; Watson, A.J. A Greenland Sea perspective on the dynamics of postconvective eddies. *J. Phys. Oceanogr.* **2008**, *38*, 2755–2771. [[CrossRef](#)]
19. Serra, N.; Sadux, S.; Ambar, I. Observations and laboratory modeling of meddy generation of cape St. Vincent. *J. Phys. Oceanogr.* **2002**, *32*, 3–25. [[CrossRef](#)]
20. Shaw, P.-T.; Chao, S.-Y. Effects of a baroclinic current on a sinking dense water plume from a submarine canyon and heton shedding. *Deep Sea Res. Part I* **2003**, *50*, 357–370. [[CrossRef](#)]
21. Messori, G. The Sporadic Nature of Meridional Heat Transport in the Atmosphere. Ph.D. Thesis, Imperial College London, London, UK, 2013; p. 217.
22. Mokhov, I.I.; Gryanik, V.M.; Doronina, T.N.; Lagun, D.E.; Mokhov, O.I.; Naumov, E.P.; Petukhov, V.K.; Tevs, M.V.; Khairullin, R.R. *Vortex Activity in the Atmosphere: Tendencies of Changes*; Institute of Atmospheric Physics of RAS: Moscow, Russia, 1993; 97p.
23. Mokhov, I.I.; Doronina, T.N.; Gryanik, V.M.; Khairullin, R.R.; Korovkina, L.V.; Lagun, V.E.; Mokhov, O.I.; Naumov, E.P.; Petukhov, V.K.; Senatorsky, A.O.; et al. Extratropical cyclones and anticyclones: Tendencies of change. In *The Life of Extratropical Cyclones*; Gronas, S., Shapiro, M.A., Eds.; Geophysical Institute, University of Bergen: Bergen, Norway, 1994; Volume 2, pp. 56–60.
24. Pedlosky, J. The instability of continuous heton clouds. *J. Atmos. Sci.* **1985**, *42*, 1477–1486. [[CrossRef](#)]
25. Griffiths, R.W.; Hopfinger, E.J. Experiments with baroclinic vortex pairs in a rotating fluid. *J. Fluid Mech.* **1986**, *173*, 501–518. [[CrossRef](#)]
26. Griffiths, R.W.; Hopfinger, E.J. Coalescing of geostrophic vortices. *J. Fluid Mech.* **1987**, *178*, 73–97. [[CrossRef](#)]
27. Helfrich, K.R.; Battisti, T.M. Experiments on baroclinic vortex shedding from hydrothermal plumes. *J. Geophys. Res.* **1991**, *96*, 12511–12518. [[CrossRef](#)]
28. Thivolle-Cazat, E.; Sommeria, J.; Galmiche, M. Baroclinic instability of two-layer vortices in laboratory experiments. *J. Fluid Mech.* **2005**, *544*, 69–97. [[CrossRef](#)]
29. Danilov, S.; Gryanik, V.; Olbers, D. *Equilibration and Lateral Spreading of a Strip-Shaped Convection Region*; Report 86; Alfred-Wegener-Institut für Polar- und Meeresforschung: Bremerhaven, Germany, 1998; p. 66
30. Danilov, S.; Gryanik, V.; Olbers, D. Equilibration and lateral spreading of a strip-shaped convection region. *J. Phys. Oceanogr.* **2001**, *31*, 1075–1087. [[CrossRef](#)]
31. Doronina, T.; Gryanik, V.; Olbers, D.; Warncke, T. *A 3D Heton Mechanism of Lateral Spreading in Localized Convection in a Rotating Stratified Fluid*; Report 87; Alfred-Wegener-Institut für Polar- und Meeresforschung: Bremerhaven, Germany, 1998; 84p.
32. Gryanik, V.M.; Doronina, T.N.; Olbers, D.; Warncke, T.H. The theory of three-dimensional hetons and vortex-dominated spreading in localized turbulent convection in a fast rotating stratified fluid. *J. Fluid Mech.* **2000**, *423*, 71–125. [[CrossRef](#)]
33. Gryanik, V.M.; Borth, H.; Olbers, D. *The Theory of Quasigeostrophic von Kármán Vortex Streets in Two-Layer Fluids on Beta-Plane and Intermittent Turbulent Jets*; Alfred-Wegener-Institut für Polar- und Meeresforschung: Bremerhaven, Germany, 2001; Volume 106, 59p.
34. Gryanik, V.M.; Borth, H.; Olbers, D. The theory of quasigeostrophic von Kármán vortex streets in two-layer fluids on beta-plane. *J. Fluid Mech.* **2004**, *505*, 23–57. [[CrossRef](#)]
35. Gryanik, V.M.; Doronina, T.N. Advective transport of a conservative solute by baroclinic singular quasigeostrophic vortices in the atmosphere (ocean). *Izvestiya Atmos. Ocean. Phys.* **1990**, *26*, 1011–1026.
36. Lim, C.C.; Majda, A.J. Point vortex dynamics for coupled surface/interior QG and propagating heton clusters in models for ocean convection. *Geophys. Astrophys. Fluid Dyn.* **2001**, *94*, 177–220. [[CrossRef](#)]

37. Marshall, J.S. Chaotic oscillations and breakup of quasigeostrophic vortices in the N -layer approximation. *Phys. Fluids* **1995**, *7*, 983–992. [[CrossRef](#)]
38. Jamaloodeen, M.I.; Newton, P.K. Two-layer quasigeostrophic potential vorticity model. *J. Math. Phys.* **2007**, *48*, 48. [[CrossRef](#)]
39. Reznik, G.; Kizner, Z. Two-layer quasi-geostrophic singular vortices embedded in a regular flow: 1. Invariants of motion and stability of vortex pairs. *J. Fluid Mech.* **2007**, *584*, 185–202. [[CrossRef](#)]
40. Reznik, G.; Kizner, Z. Two-layer quasi-geostrophic singular vortices embedded in a regular flow: 2. Steady and unsteady drift of individual vortices on a beta plane. *J. Fluid Mech.* **2007**, *584*, 203–223. [[CrossRef](#)]
41. Shteinbuch-Fridman, B.; Makarov, V.; Kizner, Z. Transitions and oscillatory regimes in two-layer geostrophic hetons and tripoles. *J. Fluid Mech.* **2017**, *810*, 535–553. [[CrossRef](#)]
42. Sokolovskiy, M.A.; Verron, J. Finite-core hetons: Stability and interactions. *J. Fluid Mech.* **2000**, *423*, 127–154. [[CrossRef](#)]
43. Young, W.R. Some interactions between small numbers of baroclinic, geostrophic vortices. *Geophys. Astrophys. Fluid Dyn.* **1985**, *33*, 35–61. [[CrossRef](#)]
44. Kozlov, V.F.; Makarov, V.G.; Sokolovskiy, M.A. Numerical model of the baroclinic instability of axially symmetric eddies in two-layer ocean. *Izvestiya Atmos. Ocean. Phys.* **1986**, *22*, 674–678.
45. Helfrich, K.R.; Send, U. Finite-amplitude evolution of two-layer geostrophic vortices. *J. Fluid Mech.* **1988**, *197*, 331–348. [[CrossRef](#)]
46. Polvani, L.M.; Zabusky, N.J.; Flierl, G.R. Applications of contour dynamics to two-layer quasi-geostrophic flows. *Fluid Dyn. Res.* **1988**, *3*, 422–424. [[CrossRef](#)]
47. Polvani, L.M. Two-layer geostrophic vortex dynamics. 2. Alignment and two-layer V-states. *J. Fluid Mech.* **1991**, *225*, 241–270. [[CrossRef](#)]
48. Reinaud, J.N. On the stability of continuously stratified quasi-geostrophic hetons. *Fluid Dyn. Res.* **2015**, *47*, 035510. [[CrossRef](#)]
49. Kizner, Z. Stability and transitions of hetonic quartets and baroclinic modons. *Phys. Fluids* **2006**, *18*, 056601 [[CrossRef](#)]
50. Makarov, V.G.; Sokolovskiy, M.A.; Kizner, Z. Doubly symmetric finite-core heton equilibria. *J. Fluid Mech.* **2012**, *708*, 397–417. [[CrossRef](#)]
51. Reinaud, J.; Carton, X. The stability and the nonlinear evolution of quasi-geostrophic hetons. *J. Fluid Mech.* **2009**, *636*, 109–135. [[CrossRef](#)]
52. Reinaud, J.N.; Carton, X. Head on collisions between two quasi-geostrophic hetons in a continuously stratified fluid. *J. Fluid Mech.* **2015**, *779*, 144–180. [[CrossRef](#)]
53. Reinaud, J.N.; Carton, X.; Dritschel, D.G. Interaction between a quasi-geostrophic buoyancy filament and a heton. *Fluids* **2017**, *2*, 37. [[CrossRef](#)]
54. Ryzhov, E.A.; Sokolovskiy, M.A. Interaction of two-layer vortex pair with a submerged cylindrical obstacle in a two-layer rotating fluid. *Phys. Fluids* **2016**, *28*, 056602. [[CrossRef](#)]
55. Sokolovskiy, M.A.; Carton, X. Baroclinic multipole formation from heton interaction. *Fluid Dyn. Res.* **2010**, *42*, 045501. [[CrossRef](#)]
56. Sokolovskiy, M.A.; Koshel, K.V.; Verron, J. Three-vortex quasi-geostrophic dynamics in a two-layer fluid. Part I. Analysis of relative and absolute motions. *J. Fluid Mech.* **2013**, *717*, 232–254. [[CrossRef](#)]
57. Sokolovskiy, M.A.; Verron, J. *Dynamics of Vortex Structures in a Stratified Rotating Fluid*; Atmospheric and Oceanographic Sciences Library; Springer: Cham, Switzerland, 2014; Volume 47, p. 382.
58. Sokolovskiy, M.; Verron, J.; Carton, X.; Gryanik, V. On instability of elliptical hetons. *Theor. Comput. Fluid Dyn.* **2010**, *24*, 117–123. [[CrossRef](#)]
59. Valcke, S.; Verron, J. On interactions between two finite-core hetons. *Phys. Fluids* **1993**, *A5*, 2058–2060. [[CrossRef](#)]
60. Verron, J.; Valcke, S. Scale-dependent merging of baroclinic vortices. *J. Fluid Mech.* **1994**, *264*, 81–106. [[CrossRef](#)]
61. Sokolovskiy, M.A.; Koshel, K.V.; Dritschel, D.G.; Reinaud, J.N. N -symmetric interaction of N hetons. I: Analysis of the case $N = 2$. *Phys. Fluids* **2020**, *32*, 096601. [[CrossRef](#)]
62. Koshel, K.V.; Reinaud, J.N.; Riccardi, G.; Ryzhov, E.A. Entrapping of a vortex pair interacting with a fixed point vortex revisited. I. Point vortices. *Phys. Fluids* **2018**, *30*, 096603. [[CrossRef](#)]
63. Reinaud, J.N.; Koshel, K.V.; Ryzhov, E.A. Entrapping of a vortex pair interacting with a fixed point vortex revisited. II. Finite size vortices and the effect of deformation. *Phys. Fluids* **2018**, *30*, 096604. [[CrossRef](#)]
64. Simó, C. New families of solutions to the N -body problems. In *European Congress of Mathematics: Barcelona, July 10–14, 2000, Volume I*; Casacuberta, C., Miró-Roig, R.M., Verdera, J., Xambó-Descamps, S., Eds.; Progress in Mathematics; Birkhäuser Basel: Basel, Switzerland, 2001; Volume 201, pp. 101–115.
65. Borisov, A.V.; Mamaev, I.S.; Kilin, A.A. Absolute and relative choreographies in the problem of point vortices moving on a plane. *Regul. Chaotic Dyn.* **2004**, *9*, 101–111. [[CrossRef](#)]
66. Borisov, A.V.; Kilin, A.A.; Mamaev, I.S. The dynamics of vortex rings: Leapfrogging, choreographies and the stability problem. *Regul. Chaotic Dyn.* **2013**, *18*, 33–62. [[CrossRef](#)]
67. Bartsch, T. Periodic solutions of singular first-order Hamiltonian systems of N -vortex type. *Arch. Math.* **2016**, *107*, 413–422. [[CrossRef](#)]
68. Calleja, R.C.; Doedel, E.J.; García-Azpeitia, C. Choreographies in the n -vortex problem. *Regul. Chaotic Dyn.* **2018**, *23*, 595–612. [[CrossRef](#)]
69. Dai, Q.; Gebhard, B.; Bartsch, T. Periodic solutions of N -vortex type Hamiltonian systems near the domain boundary. *SIAM J. Appl. Math.* **2018**, *78*, 977–995. [[CrossRef](#)]

-
70. Dritschel, D.G. Contour surgery: A topological reconnection scheme for extended integrations using contour dynamics. *J. Comput. Phys.* **1988**, *79*, 240–266. [[CrossRef](#)]
 71. NIST Digital Library of Mathematical Functions. Available online: <https://dlmf.nist.gov/>.

Disclaimer/Publisher’s Note: The statements, opinions and data contained in all publications are solely those of the individual author(s) and contributor(s) and not of MDPI and/or the editor(s). MDPI and/or the editor(s) disclaim responsibility for any injury to people or property resulting from any ideas, methods, instructions or products referred to in the content.